Arab American University-Palestine

Faculty of Graduate Studies

Characterization of Arsenic doped MOS_2 powders

By

Nancy Asem (Mahmood Husni) Jaradat

Supervisor

Prof. Dr. Atef Qasrawi

This thesis was submitted in partial fulfillment of the requirement for the Master's degree in Physics

January/2023

Characterization of Arsenic doped MOS_2 powders

By

Nancy Asem (Mahmood Husni) Jaradat

This thesis was defended successfully on ١٩ January 2023 and approved by:

Committee members	Signature
1. Supervisor Prof. Dr. Atef Fayez Qasrawi	.....
2. External Examiner Assoc. Prof. Dr. Iyad Saadeddin	.....
3. Internal Examiner Prof. Dr. Hazem Khanfar	.....

Declaration

The work in this thesis, unless otherwise referenced, is the researcher's own work and has not been submitted elsewhere for any other degree or qualification.

Student's Name: Nancy Asem (Mahmood Husni) Jaradat

Signature: 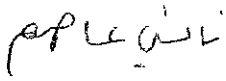

Date: 30/7/2023

Student ID:202012900

Acknowledgments

In the name of God, the Most Merciful. My master's thesis has been completed from my beautiful university, the Arab American University thanks to God. My special thanks go to all faculty members. In particular, the wonderful Professor Dr. Atef Qasrawi, who has moved me in the spirit of defiance and determination to pursue my work in a period when I had become bored and exhausted. I also thanks to the external examiner, and the internal examiner. They made wonderful efforts in my thesis to appear in its final form. I am honored to discuss my thesis with them. All love and thanks to my beautiful family for supporting me all the time. My husband Qutaiba Jaradat (Abu Maryam) who was harnessed by God to support and encourage me.

I would also like to thank the assistance Rana Daragmeh for her unlimited support in the laboratory. My smart friend Lamiaa Fashafsha, we walked together on the path of learning to success. Thank you to everyone who helped completed this work.

Abstract

In this work, molybdenum sulfide powders are doped with arsenic by the solid state reaction technique. The doped powders are characterized by the X-ray diffraction, scanning electron microscopy, energy dispersive X-ray spectroscopy, impedance spectroscopy and current-voltage characteristics techniques. Various doping contents in accordance with the formula $MoAs_xS_2$. The weight ratio (x) of arsenic in the samples is varied in the range of $0.00 - 0.80$. The doped samples were then sintered at $200\ ^{\circ}C$ for 20 hours in the air atmosphere. It is observed that the larger the arsenic content in the samples the smaller the crystallite sizes, the larger the microstrain, the larger the defect density and the larger the stacking faults percentages. As Sintering the samples at $200\ ^{\circ}C$ did not alter the trend of variation of the structural parameters. In addition, the increase in the As content in the MoS_2 powders is observed to increase the pores. Accumulation of As grains started appearing on the surface of the samples as x exceeds 0.40. On the other hand, the electrical measurement has shown that the electrical resistivity increases with increasing As content in the samples. The temperature dependent electrical resistivity measurements has shown that the activation energy ($E\sigma$) of free charge carriers in regions where thermionic emission is dominant increased. On the other hand, in regions where variable ranges hopping dominates the degree of electronic state disorder and the variable range hopping distance increased while the density of localized states near Fermi levels decreased with increasing arsenic content. Moreover, the impedance spectroscopy studies have shown that the doped and undoped MoS_2 samples can exhibit negative conductance effect. Negative conductance effect which is engineered by As content is beneficial for fabrication of microwave devices useful in communication technology.

List of contents

List of tables

List of Figures

Chapter One
Introduction

Recent investigations on molybdenum disulfide (MoS_2) have shown that this material is a two-dimensional layered inorganic compound with many extraordinary properties in crystalline mineral [1]. It is important in the area of energy storage and environmental remediation [2]. It is used for various functional applications, it is reported to have applications in photo catalysts, supercapacitors and membrane for environmental applications [1]. It has a very important thermoelectric applications in nanosheets [3] and light-driven antibacterial application in MoS_2 nanoflowers [4]. It is also uses as a molecular polymer sensor for the electrochemical detection of rutin [5]. As heterojunction element, MoS_2 appears to be attractive in mixed-dimensional heterojunctions. The Phthalocyanines/MoS_2 heterojunctions is observed to be suitable for range-separated hybrid functional [6]. In addition, MoS_2/Ni substrates are mentioned to being attractive for binder-free methanol electro-oxidation application [7]. The MoS_2 nanosheets by green chemistry technique has application in triboelectric and catalytic energy harvesting [8]. Furthermore, The MoS_2 monolayer by chemical vapor deposition technique has photodetection application [9].

The MoS_2 has several techniques for thin film preparation from MoS_2 based bulk material. The pulsed laser deposition technique was used for high performance UV/ MoS_2 photodetector [10]. Moreover, ZnO/ MoS_2 nanosheets was used surface photo voltage technique to enhance ultraviolet light gas sensitive activity [11]. In addition, it was used 2-D MoS_2/TiO_2 nanocomposite to remove and degrade of mixed dye pollutants with integrated adsorption-photo catalysis technique [12]. The polarimetry technique was used to investigate optical beam shifts in MoS_2 monolayer [13].

Furthermore, the Ritz Galerkin Finite element technique was used to investigate of quantum confinement effects on MoS_2 based transistor [14]. The electrolysis deposition and powder metallurgy technique was used to find microstructure and tribology properties of the (Cu/MoS_2)/graphene nanocomposite [15]. In addition, the Z-scan technique was used to find non-linear thermo-on optical properties of MoS_2 Nano flakes [16]. For supercapacitor application MoS_2/CeO_2 heterostructure, it was prepared by Facile Hydrothermal Technique [17]. To improve performances of MoS_2 phototransistors, it was used the encapsulation [18]. Nanosheets, nanoflowers and nanocomposites based on MoS_2 were used as potential adsorbents [1].

The MoS_2 has a unique properties, it has a high specific surface area and structurally adjustable band structure [19]. The structural property is creating dissipative currents in the MoS_2 [20]. the structural and optical properties are significantly temperature-dependent of 2D-MoS_2 layers [21]. The inherent structural characteristics of MoS_2 can enhance of tribological properties by making them dispersible in lube media [22]. The relationship between the optical properties and surface chemistry of MoS_2 quantum dots has very important, it has been revealing the important role of surface ligands to define the absorption band gap and luminescence quantum yields [23]. The optical properties of AlN (Aluminium nitride)/MoS_2 heterostructure show that the absorption coefficient exhibits enhancement in their characteristic [24]. The MoS_2/WSSe (where W: Tungsten, S:Sulfer and Se: Selenium) van der Waals heterojunctions was design of multi-functional high-performance electronic and optoelectronic devices [25]. A strong absorption in the NIR-IR have been observed in Monolayer MoS_2 [26]. It is mentioned that the existence of wrinkles in MoS_2 can affect the electrical properties [27]. The strain of MoS_2 is an important and use to tune the electrical properties of 2D materials

and can be used to engineer high-efficiency electrical contacts [28]. The Au/MoS_2 charges transport channels introduces tunable localized Schottky barrier landscape and controls the electronic properties [29].

Due to novel feature of molybdenum disulfide, here in this work, we are motivated to study structural and electrical properties of MoS_2. However, MoS_2 is very defective material and its defect density is relatively high. The large defect concentration make many limitations of the technology application. The defect density can be reduced by doping MoS_2 with material of low ionic radius to replace vacant sites. The most appropriate material is arsenic. Particularly, five levels of doping will be studied. The modification in the structural and electrical properties will be monitored.

Chapter Two
Theoretical Background

2.1 The X-ray diffraction

X-ray diffraction is a phenomenon where the atomic planes of a crystal cause an incident beam of X- rays to make interference with one another (Fig.2.1) as they leave the crystal so it is a technique to find characterizing crystalline materials. X-ray was generated by a cathode ray tube, filtered to produce monochromatic radiation, collimated to concentrate, and directed toward the sample [30].

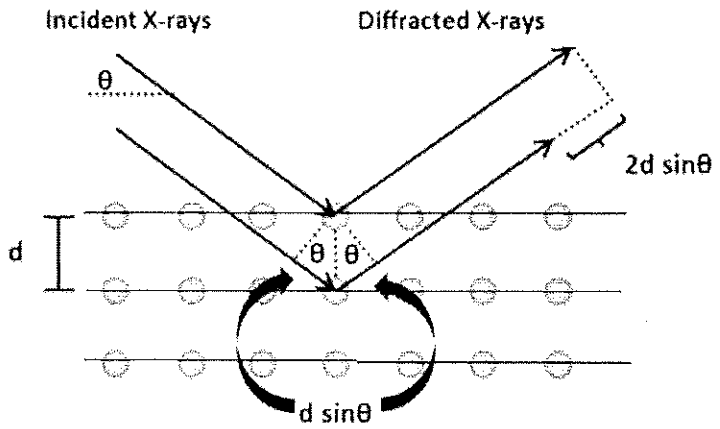

Fig. 2.1: The schematic diagram of the X-ray diffraction.

2.1.1 Bragg's law

X-ray onto a crystal surface with angle of incidence (θ) will reflect with the same angle (θ). When the path difference ($2dsin\theta$) between two constructive beams (Fig.2.1) is equal to an integer (n) multiple of the wavelength (λ), constructive interference will occur.

The interplaner distance (d) between two plans of atoms calculated from Bragg equation [31]:

$$2d\ sin\theta\ = n\lambda \qquad (2.1)$$

Where n is an order of reflection (positive integer), λ is the wavelength of x-rays and θ is the angle of incidence.

2.1.2 Structural properties

X-ray diffraction (XRD) provides us information about the structures, crystal orientations and other parameters, such as interplaner distance (d), crystallite size (D), strain (ε) stacking faults percent $(SF\%)$ and dislocation density (δ). All of these structural properties of the most intensive peak from the broadening width $\beta(FWHM)$ following relations [32].

Crystallite size (D); is the diameter of an individual crystallite in a crystal.

$$D = \frac{0.94\lambda}{COS\ \theta\ \beta} \quad (2.2)$$

Strain (Ɛ): is the ratio of change (contraction or expansion) in bonds lengths to the original bonds' lengths.

$$\text{Ɛ} = \frac{\beta}{4tan\theta} \quad (2.3)$$

Dislocation density (δ) : is a measure of the total length of dislocation lines in a unit area of crystalline material (line/cm^2).

$$\delta = \frac{15\text{Ɛ}}{aD} \quad (2.4)$$

Where ε is the strain, D is the crystallite grain size *and* a is the lattice constant in a-axis.

Stacking faults SF : is a type of defect in disordering of crystallographic planes. (plane defect) or it is the error in the order of the sequential layering of the planes in a crystal.

$$SF = \frac{2\pi^2\beta}{45\sqrt{3tan\theta}} \quad (2.5)$$

2.1.3 Crystallography

Crystallography is the science of the arrangement of atoms in 3-D. Crystals have one or many of the structural phases. There are seven crystal structures with 14 Braves lattice in 3-dimentional configurations [33]. These systems include triclinic, monoclinic, orthorhombic, tetragonal, cubic, trigonal. and hexagonal. They are defined in the terms of relationships between lattice angles (α, β, γ) and lattice constants(a, b, c). The crystal structures are represented in Table 2.1.

Table 2.1 The 3-D crystal structures and their conditions.

Crystal structure	Conditions	Number of Braves lattice
Triclinic	$a_1 \neq a_2 \neq a_3$, $\alpha \neq \beta \neq \gamma \neq 90^0$	1
Monoclinic	$a_1 \neq a_2 \neq a_3$, $\alpha = \gamma = 90^0 \neq \beta$	2
Orthorhombic	$a_1 \neq a_2 \neq a_3$, $\alpha = \beta = \gamma = 90^0$	4
Tetragonal	$a_1 = a_2 \neq a_3$, $\alpha = \beta = \gamma = 90^0$	2
Cubic	$a_1 = a_2 = a_3$, $\alpha = \beta = \gamma = 90^0$	3
Trigonal	$a_1 = a_2 = a_3$, $\alpha = \beta = \gamma < 120^o \neq 90^0$	1
Hexagonal	$a_1 = a_2 \neq a_3$, $\alpha = \beta = 90^0$, $\gamma = 120^o$	1

The triclinic crystal system is the most disordered of all of these systems and it is a one-fold symmetry. Three axes of different unit cell, all having different angles, and none of angles is equal to 90 degrees. The interplaner distance in accordance with given peak is given with the following equation [34]:

$$\frac{1}{d^2} = \frac{1}{V^2}(s_{11}h^2 + s_{22}k^2 + s_{33}l^2 + 2s_{12}hk + 2s_{23}kl + 2s_{13}hl) \qquad (2.6)$$

Where d is the inter-planner distance, V is the volume of the crystal (h, k, l) is the miler indices, as we can see from Fig.2.2, s_{11} is the direct stress acting on the positive and negative 1 faces in the 1-axis direction and we can write the equation as: $s_{11} = b^2c^2sin\alpha^2$, s_{22} is the direct stress acting on the positive and negative 2 faces in the 2-axis direction and we can write the equation as: $s_{22} = a^2c^2sin\beta^2$, s_{33} is the direct stress acting on the positive and negative 3 faces in the 3-axis direction and we can write the equation as: $s_{33} = a^2b^2sin\gamma^2$, s_{12} is the shearing stress acting on the positive and negative 1 faces in the 2-axis direction and acting on the positive and

negative 2 faces in the 1-axis direction and we can write the equation as: $s_{12} = abc^2(cos\alpha\ cos\beta - cos\gamma)$, s_{23} is the shearing stress acting on the positive and negative 2 faces in the 3-axis direction and acting on the positive and negative 3 faces in the 2-axis direction and we can write the equation as: $s_{23} = a^2bc(cos\beta\ cos\gamma - cos\alpha)$ and s_{13} is the shearing stress acting on the positive and negative 1 faces in the 3-axis direction and acting on the positive and negative 3 faces in the 1-axis direction and we can write the equation as: $s_{13} = ab^2c(cos\gamma\ cos\alpha - cos\beta)$ [34].

I will derive the monoclinic equation from the triclinic equation by doing some abbreviations related to the properties of the monoclinic structure ($\alpha = \gamma = 90^0 \neq \beta$). So we have $s_{11} = b^2c^2$, $s_{22} = a^2c^2sin\beta^2$, $s_{33} = a^2b^2$, $s_{12} = 0$, $s_{23} = 0$, $s_{13} = \_ab^2c\ cos\beta$ and $V = abc\ sin\beta$. Substituting the s_{xx} values into equation (2.6), The following monoclinic structure equation is obtained:

$$\frac{1}{d^2} = \frac{1}{sin\beta^2}\left(\frac{h^2}{a^2} + \frac{k^2 sin\beta^2}{b^2} + \frac{l^2}{c^2} + \frac{2hl\ cos\beta}{ac}\right) \qquad (2.7)$$

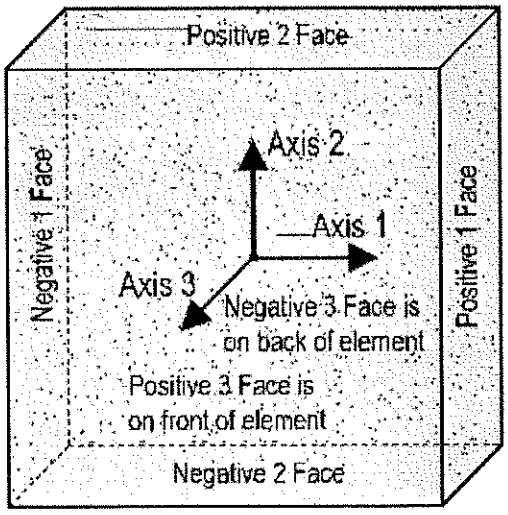

Fig. 2.2: The positive and negative faces in the 1, 2 and 3-axes.

Each system has an interplaner distance (d). This quantity is a perpendicular distance between two successive planes in a family of miller indices (hkl). It can be used to uniquely identify the plane of surfaces.

2.1.4: Deformation in materials

The free energy of a crystalline material is increased during deformation due to the presence of dislocation and interfaces [35]. The material is thermodynamically unstable when it contains defects. When the material is annealed, the microstructures and the properties of the material are changed [36]. The grains shape will also change which lead to an increase in the area of the total grain boundary [37]. Moreover, as the strain and dislocations increased in the material, the stored energy will increase [38].

2.2: Impedance spectroscopy

It is an electrical circuit consisting of a resistor (R), capacitor (C) and inductor (L) connected in series or in parallel. RLC circuit is performed. Impedance spectroscopy for RLC circuits is performed when AC signals are provided using a voltage source.

2.2.1: Series RLC

The series RLC circuit (Fig. 2.3) has a single loop with the current have the same value for each circuit element. The magnitude of the source voltage (V_S) distributed on elements making the three voltages, V_R, V_L and V_C.

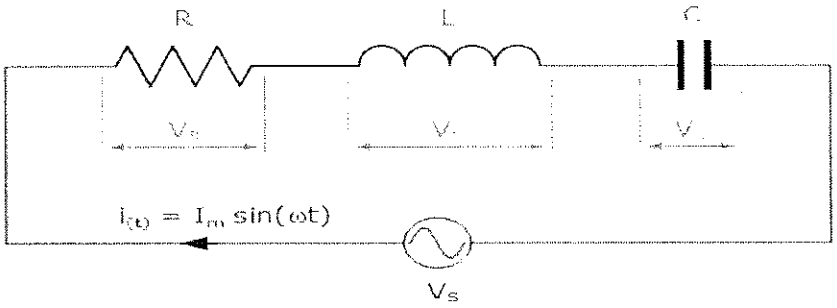

Fig. 2.3 The series RLC circuit analysis.

The magnitude voltages of V_R, V_L and V_C are given by the following equations:

$$V_R = IR \tag{2.8}$$

$$V_L = IX_L = IwL \tag{2.9}$$

$$V_C = IX_C = \frac{\mathrm{I}}{\mathrm{wc}} \tag{2.10}$$

Where I is the current of the circuit, R is the resistance in the circuit, $X_L$is the inductive reactance, X_C is the capacitive reactance in circuit, ω is the angular frequency of the source and equal $(2\pi f)$, C is the capacitance and L is the inductance in the circuit.

By applying Kirchhoff's voltage law (KVL), which states that the algebraic sum of the potential differences in any loop must be equal to zero [39], so the sum of the three voltages will give us the amplitude of the source voltage (V_S):

$$V_S - V_R - V_L - V_C = 0 \tag{2.10}$$

$$V_S - IR - IwL - \frac{\mathrm{I}}{\mathrm{wc}} = 0 \tag{2.12}$$

$$V_S = IR + IwL + \frac{\mathrm{I}}{\mathrm{wc}} \tag{2.13}$$

The voltage triangle on phasor diagram (Fig. 2.4) for a series RLC circuit gives that:

$$V_S = \sqrt{{V_R}^2 + \overline{(V_L - V_C)^2}} = I\sqrt{R^2 + (X_L - X_c)^2} = IZ \tag{2.14}$$

where Z is the total impedance of the circuit.

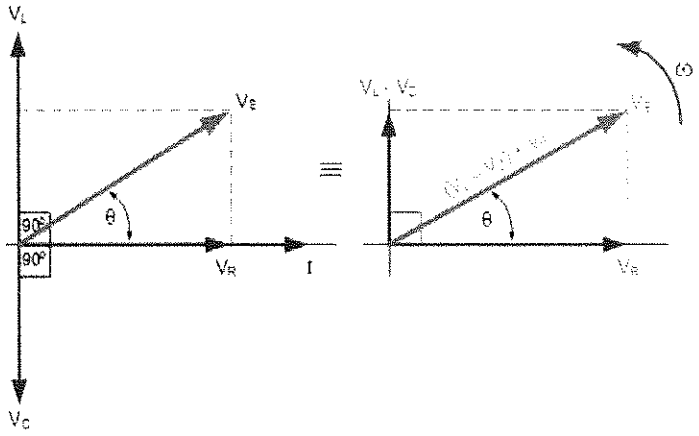

Fig. 2.4: The impedance triangle phase diagram of series RLC circuit.

2.2.2: Parallel RLC

In the parallel RLC circuit, the applied voltage is common to all components of the RLC circuit and the source current (I_S) is the vector sum of the currents through each element current I_R, I_L and I_C . Fig. 2.5 shows a diagram of parallel RLC circuit.

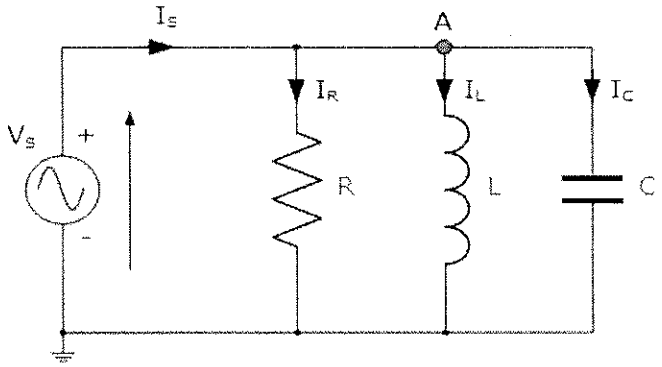

Fig. 2.5: The parallel LRC circuit diagram.

The current through each branch is found by applying Kirchhoff's current law, which states states that the algebraic sum of all currents entering and exiting a node must equal zero [40]. Thus, the currents entering and leaving node "A" above (Fig. 2.5) are given by:

$$I_S = I_R + I_L + I_C \tag{2.15}$$

and the current Triangle on phasor diagram (Fig. 2.6) for a parallel RLC Circuit gives that:

$$I_S = \sqrt{{I_R}^2 + (I_L - I_C)^2} = \sqrt{(\frac{V}{R})^2 + (\frac{V}{X_L} - \frac{V}{X_C})^2} = \frac{V}{Z} \tag{2.16}$$

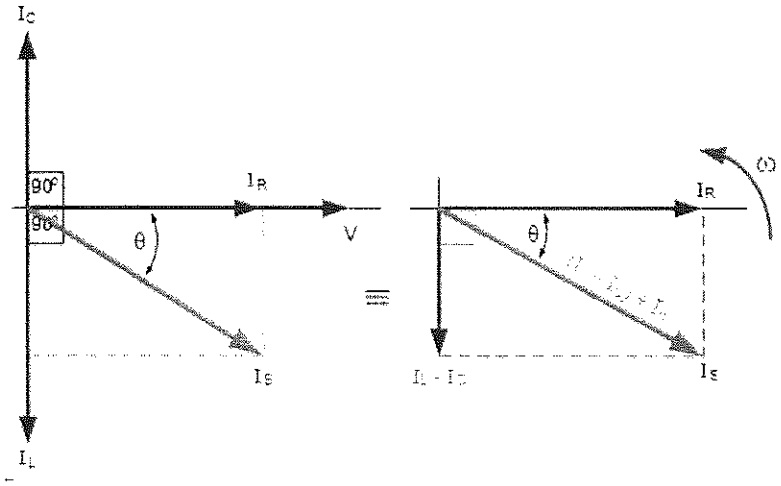

Fig. 2.6: The current triangle phase diagram for a parallel RLC circuit.

2.2.3: Ac conduction in solids

The alternating current (AC) conductivity spectra is referred to the quantum mechanical tunneling (QMT) or could be referred to correlated barrier hopping conduction (CBH) or may be variant of the two [41]. Conductance of the solid material can be obtained from the following relation:

$$G = \sigma \frac{A}{L} \tag{2.17}$$

Where σ is the conductivity, L is the length of a conductor and A is the cross sectional area. The conductivity is a function of frequency [41] following the relation,

$$\sigma(w) = Aw^s \tag{2.18}$$

Where A is the constant dependent on the temperature, w is the frequency and s is the exponent (less than or equal to unity). The conductivity appears if the mechanism of loss has a wide range of a relaxation times (τ). If the distribution of a relaxation times ($n(\tau)$) is inversely proportional to τ, this means the exponent value $s = 1$. the relaxation time (τ) follows the relation:

$$\tau = \tau_o e^{\xi} \qquad (2.19)$$

The random variable $\xi = 2\alpha R$ when QMT dominates with R is an intersite separation and α is a spatial decay parameter that describes the localized state at each site. α is constant for all sites and equal to $0.1\,A^{o}$ [42]. The AC conductivity is given by the relation.

$$\sigma_{TUN}(w) = \frac{\pi^4 e^2 KT\alpha^{-1}\left(N(E_F)\right)^2 w R_w^2}{24} \qquad (2.20)$$

Where e is the electron charge, $N(E_F)$ is the density of the states at the Fermi level (assumed constant with varying frequency), R_w is the hopping distance at a particular frequency W, R_w is Given by the relation:

$$R_\omega = \frac{1}{2\alpha} \ln\left(\frac{1}{\omega\tau_o}\right) \qquad (2.21)$$

The logarithm for conductivity:

$$\ln\sigma(w) = \ln A + s \ln(w) \qquad (2.22)$$

The derivative for each side of the equation (2.23)

$$d\ln\sigma(w) = 0 + s\, d\ln(w) \qquad (2.23)$$

The exponent s can be found from the relation:

$$s = \frac{d\ln(\sigma(\omega))}{d\ln(\omega)} \qquad (2.24)$$

In QMT model the factor s of the DC conductivity is given by the relation:

$$s = 1 - \frac{4}{\ln(\frac{1}{\omega\tau_0})} \qquad (2.25)$$

The exponent s is frequency dependent that decreases with increasing frequency at constant temperature. When the random variable $\xi = W/k_\beta T$ with W is hopping barrier height, then CBH dominates, and the AC conductivity for CBH is given by the following relation:

$$\sigma(\omega) = \sigma_H + \left[\frac{\sigma_L - \sigma_H}{(1+\omega^2\tau^2)}\right] \qquad (2.26)$$

Where σ (L) and σ (H) means experimental conductivity at low and high frequency, respectively. It is also possible that the AC conductivity refers to both conduction mechanism QMT and CBH, then the total conductivity is given by:

$$\frac{1}{\sigma tot} = \frac{1}{\sigma QMT} + \frac{1}{\sigma CBH} \qquad (2.27)$$

2. 3 Electrical properties:

Understanding of an electrical current must begin with the nature of matter. All matter is composed of molecules and all molecules are made up of atoms, which are made up of protons, electrons, and neutrons. Electric current results when electric charges move, these may be negatively charged electrons or positive charge carriers (positive ions). There are several current mechanisms produce the flow of carriers in forward direction and the other in the reverse direction. Thermionic emission current, generation-recombination current, diffusion current and quantum tunneling current are the mechanisms of flowing the carriers [43, 44].

2.3.1: Ohm's Law (Resistance)

The fundamental properties of current and voltage are related by a property known as resistance. Voltage is applied to an electrical circuit, a current will result. The resistance will determine the amount of current that flows under a given voltage. In most cases, the resistance is reduced, the current will increase. This relation is linear for conductor and is known as Ohm's law with this relation:

$$V = I\,R \tag{2.28}$$

Where V is the potential difference measured in volts, I is the current measured in amperes, and R is the resistance measured in ohms. When the temperature of semiconductor is increased then the covalent bonds break quickly, and this works to increase the free charge carriers. So more electrons coming from the valence band to conduction band. It is clear that when the temperature increases, the conduction of semiconductor increases and resistance decreases. While in the case of a conductor, the resistivity increases with increasing temperature. So the temperature vs. resistivity property of conductor and semiconductor is completely opposite (Fig. 2.7). This may be a reason of Semiconductor does not obey Ohm's Law [45].

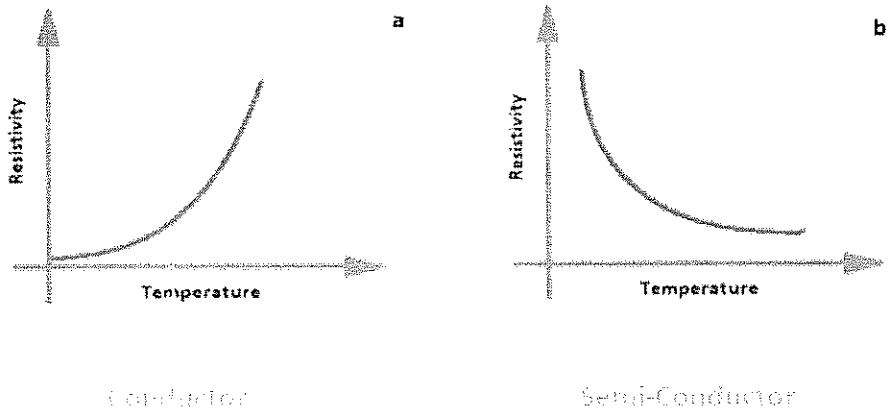

Fig. 2.7: The resistivity vs. temperature for conductor and semiconductor.

The resistance of any material is determined by four properties: length, area, material, and temperature. The resistance at any temperature is related by the relation:

$$R = \rho\, l/A \tag{2.29}$$

Where R is the resistance of a sample, ρ is the resistivity of a sample, A is the area for a sample. And L is the thickness of a sample.

2.3.2 Thermally assisted variable-range hopping

Variable-range hopping (VRH) is a model to describe carrier transport in a disordered semiconductor or amorphous solid by hopping in an extended temperature range. The electrical conductivity (σ_{th}) is mathematically defined by the relation:

$$\sigma_{th} = \sigma_o\, exp\ (-E\sigma/kT) \tag{2.30}$$

with $E_\sigma = E_c - E_F$ or $E_\sigma = E_F - E_V$, which is the electron activation energy in n-type semiconductor or the hole activation energy in p-type semiconductor, respectively. The E_F , E_c and E_V are the Fermi energy level, the conduction band energy and the valence band energy, respectively. The continuously changing E_σ with temperature (T) was attributed to the existence of VRH. The hopping conduction occurs near the Fermi level through unoccupied localized levels. When that levels is distributed quasi continuously, the hopping between two sites, when energy difference (W) is small, gets most probable. The hopping conductivity will increase by a factor of $exp\ (W / kT)$ when activation energy (E_σ) vary with temperature, $T_o > 10^3$ and $\gamma R > 1$. Where T_O is the electronic state disorder, γ is the inverse of localization

length and R is the average hopping distance. The hopping conductivity σ_{hp} with temperature (T) is given by the relation [46]:

$$\sigma_{hp}(T) = \sigma^2 \exp\left(-\left(\frac{T0}{T}\right)^{1/4}\right) \quad (2.31)$$

Where $\sigma^2 = e^2 a^2 \nu_{ph} N(E_F)$, which a is the hopping distance, $\nu_{Ph} \sim 10^{13}\ s^{-1}$ is the phonon frequency and $N(EF)$ is the density of the localized states near of the Fermi level. The degree of disorder (T_0) is given by the relation [46]:

$$T_0 = \lambda\gamma^3 / K_B N(E_F) \quad (2.32)$$

Where λ is a dimensionless constant and is equal to $18-49$ [47]. The average hopping distance (R) and the average hopping energy (W) are given by the relations [46]:

$$R = (9/8\pi\gamma K_B TN(E_F))^{1/4} \quad (2.33)$$

and

$$W = 3/4\pi R^3 N(E_F) \quad (2.34)$$

Chapter Three

Experimental Details

3.1 Pellets formation

In this work, high purity (99.9%) molybdenum disulfide (MoS_2) powder was purchased from Alfa Aeser firm. Composite made of molybdenum disulfide powder and arsenic powder to produce MoS_2: xAs . This work starts with the ball mill machine to mix arsenic with weight ratio of 0.10, 0.2 0, 0.40, 0.60 and 0.80. The ball mill which is shown in Fig. 3.1 together with the produced powders were rotated at 3000 rev/min for 15 min. All the produced powders were pressed under a pressure of 75 bar with the help of a hydraulic press machine (illustrated in Fig. 3.2) to form pellets. The diameter (D) was $11mm$ for all samples. The thicknesses of the samples (t) were $0.83mm$, $0.77\ mm$, $0.84mm$, $1.01\ mm$, $1.47mm$ and $1.11mm$, respectively. Some of the produced pellets were sintered at $200\ ^{\circ}C$ for 20 hrs. The obtained MoS_2: xAs pallets were characterized by the X-ray diffraction technique and by the scanning electron microscopy, impedance spectroscopy and temperature defendant electrical characterization are described in the following sections.

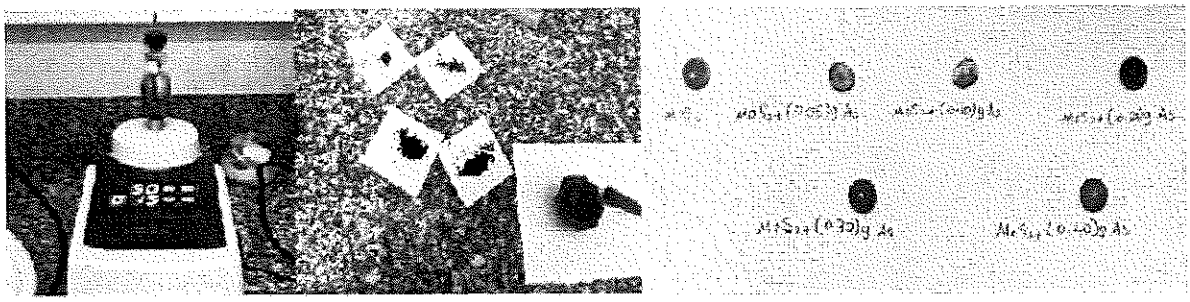

Fig. 3.1: The ball mill machine.

Fig. 3.2: The piston that make pallets.

3.2 X-ray diffraction (XRD)

The crystalline structure of MoS_2: xAs was measured by using Rigaku Miniflex 600 diffractometer operating at a wavelength equal to 1.5405 $A°$, the diffraction angles vary in the range of $10° - 70°$ at a scanning speed of $1°/min$.

A software package called "crystdiff " was used to analyze the measured XRD patterns. The lattice parameters were produced with the help of "TREOR 92" software packages. The X-ray diffraction unit which is shown in Fig. 3.3 works on the $\theta - 2\theta$ scan method illustrated in Fig. 3.4. In the figure, the sample is rotated with θ and the detector collects the diffracted beam of 2θ.

Fig. 3.3: The Rigaku Miniflex 600 diffractometer.

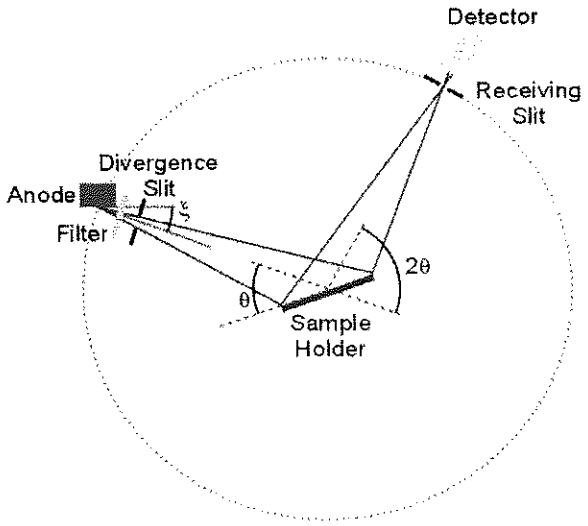

Fig. 3.4: The diagram of XRD.

3.3 Scanning electron microscopy (SEM)

Scanning electron microscopy is used to produce images of samples by the scanning of the surface with a beam of an electrons. The microscope is illustrated in Fig. 3.5. The interaction between the electron beams in Coxem 200 scanning electron microscope and the atoms in the sample producing signals include information about the shape of the surface and the composition of the samples. The diagram of SEM is presented in Fig. 3.6.

The microscope is equipped with EDAX type energy dispersive X-ray unit that can measure the composition if needed. In addition, as the schematic of the microscope presented in Fig. 3.6 shows electrons originating from the e^- gun are accelerated at 15 – 30 kV and directed by the objective lens to the sample chamber. The diffracted electron

beam is collected by the secondary detector and by the backscattered beam detector if needed.

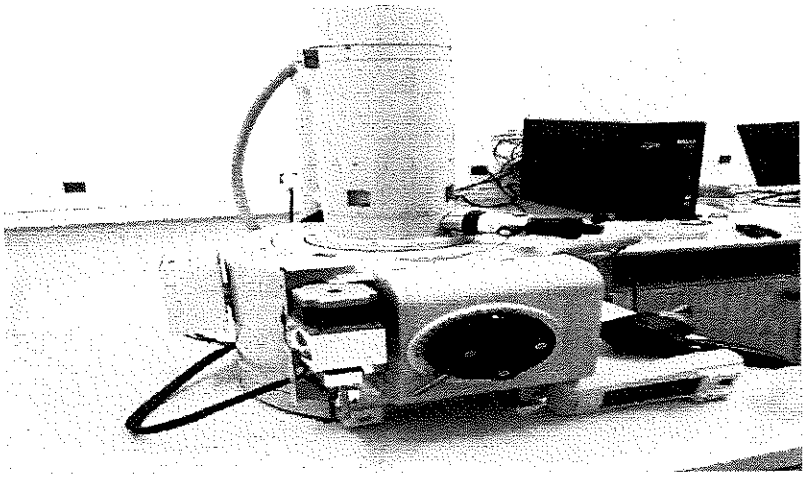

Fig. 3.5: The illustration of the SEM.

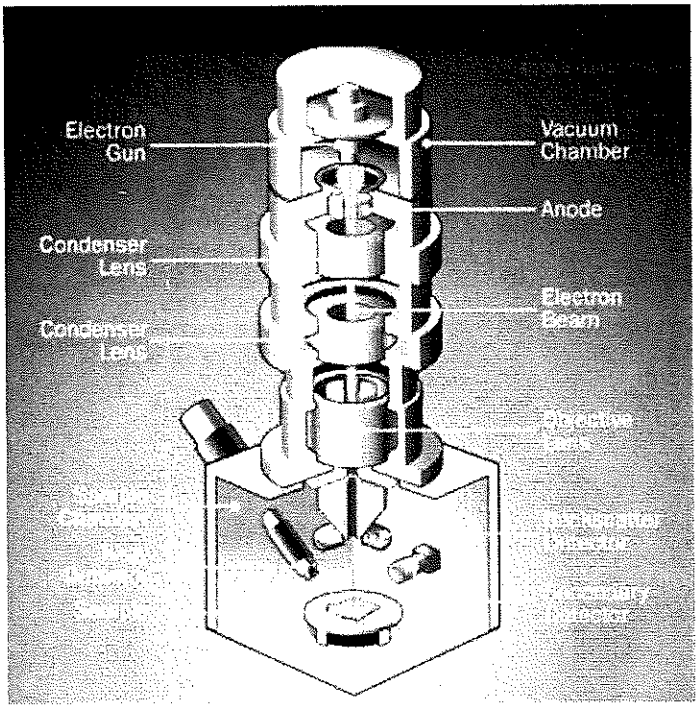

Fig. 3.6: The diagram of SEM.

3.4 Impedance spectroscopy measurements

The pressed MoS_2 pure powders and MoS_2: xAs powders are annealed at $200°C$ for 20 hrs. in a programmable oven. These samples were characterized by an impedance analyzer. The impedance analyzer works in the frequency domain of $0.1 - 1.8\,GHz$ with the help of Agilent $4291B$ $10 - 1800\,MHz$ impedance analyzer. The impedance (Z), the capacitance (C), the conductance (G), the reflection coefficient (ρ) and dielectric constant can be measured by the analyzer and collected by MATLAB software packages prior to the impedance spectra measurement, the samples are painted with silver back electrode and front point contact.

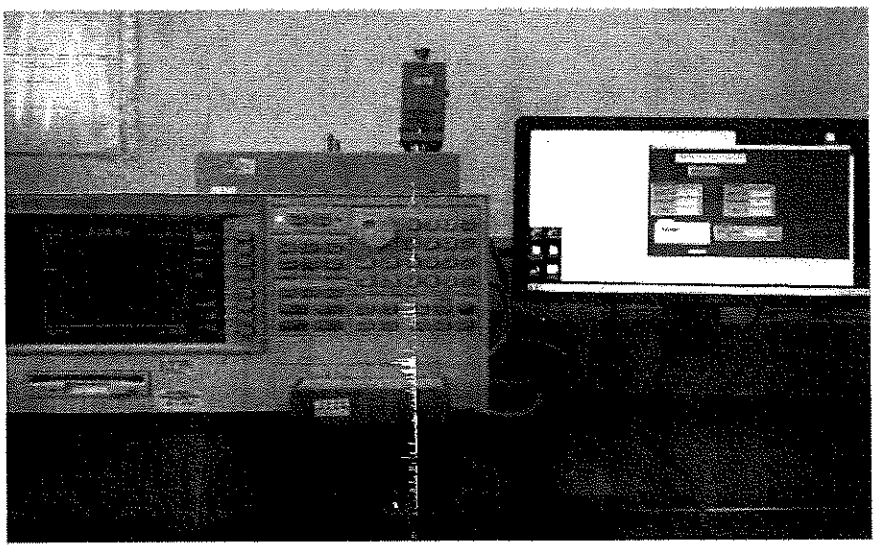

Fig. 3.7: Impedance analyzer.

3.5 Current-voltage (I-V) two point measurements:

The current (I) values were measured with respect to the applied voltage(V) for the annealed MoS_2: xAs pellets. The current-voltage characteristic was measured with the help of an automated Keithley 230 voltage source and Keithley 6485 picoammeter. The system is illustrated in Fig. 3.8.

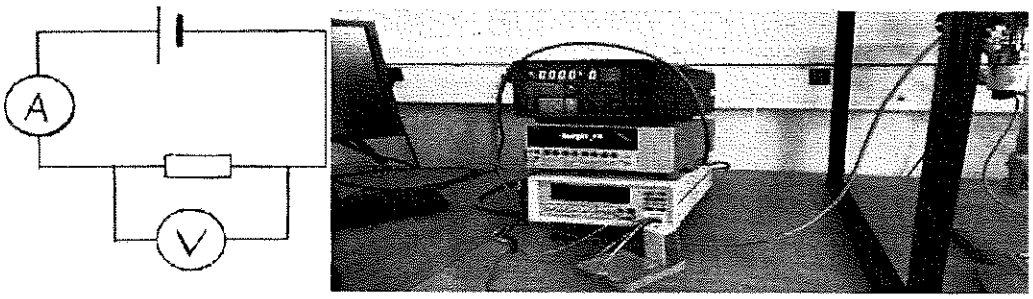

Fig. 3.8: IV measurements.

3.6 Resistivity measurement:

The temperature dependent resistivity measurements for a bars from MoS_2:xAs pellets ($Fig.3.9(a)$) with $x = 0.00, 0.10$ and 0.20 are measured in the range of $150 - 300\ K$ using a He-cryostat, where x is the weight ratio for As in MoS_2: xAs To find resistivity, we found current and voltage at each temperature for each bar using the system in Fig. 3.8. The component of cryostat which are illustrated in Fig. 3.9 are the vacuum pump ($Fig\ 3.9(b)$) and cold head ($Fig\ 3.9(c)$) supplied by a helium compressor package ($Fig\ 3.9(d)$). The helium compressor package is used as a room temperature circulator to flow the helium weight in a closed loop to the heat exchanger, the transfer line, the application heat exchanger to absorb the heat load and the cold heat exchanger. A

stainless steel -tube designed and optimized to match the required pressure drops and weight flows rate.

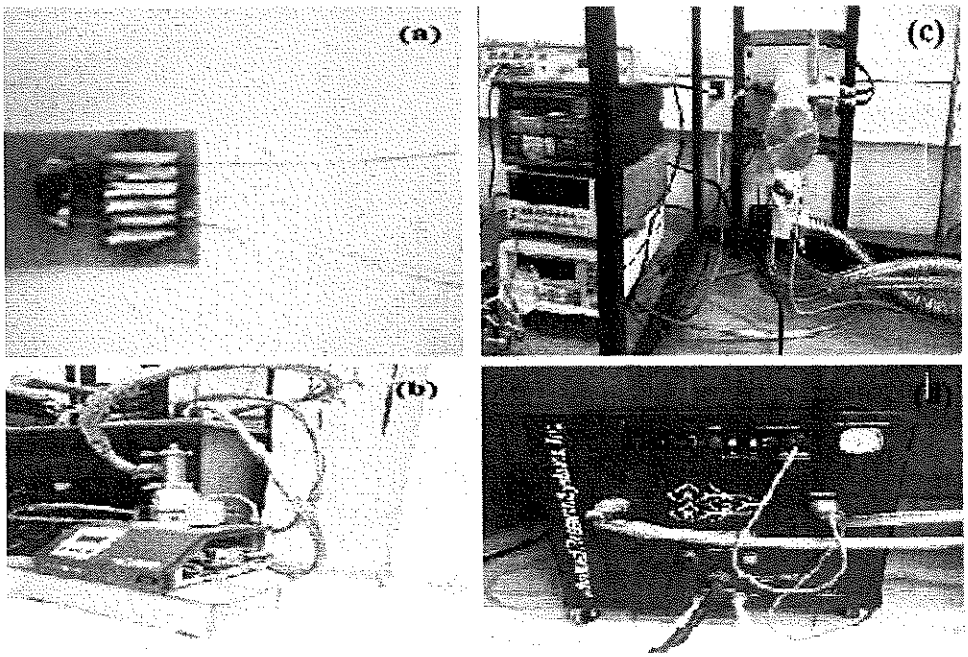

Fig. 3.9: The cryostat device.

3.7: The Hot Probe Technique:

The hot probe technique is a technique to identify the type of conductivity (p-type or n-type) of the samples. This technique consists of heated probe and a standard digital multimeter. The experiment starts by heating the soldering for a short period. After that a couple of cold probes and hot probes are attached to a pellet surface, then the hot probes connected to the positive terminal of the multimeter and heater and the cold probes connected to the negative terminal., The sample indicates that the samples under study are n-type semiconductor sample when the readable value of voltage in the multimeter is positive and p-type semiconductor sample when the readable value of voltage in the multimeter is negative. For pellets with $x = 0.00, 0.10,\ 0.20\ and\ 0.40$,

they exhibit n-type conduction and for those with $x = 0.60$ and 0.80, they exhibit p-type of conduction.

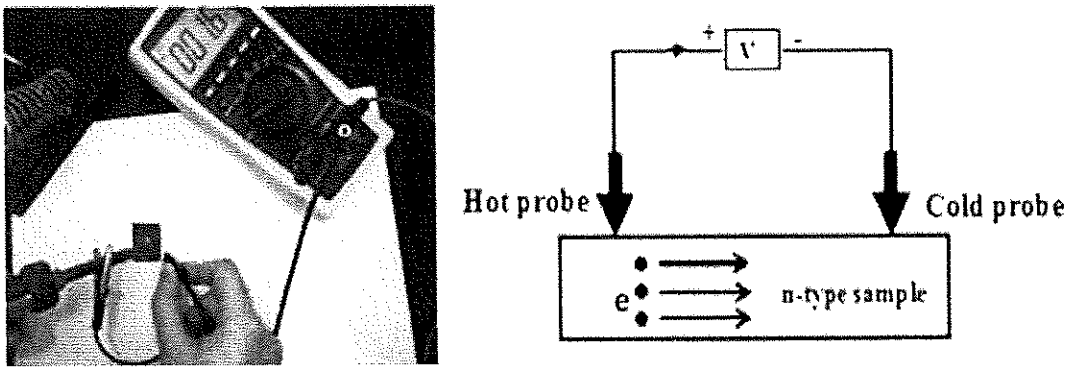

Fig. 3.10. The set-up of hot-probe technique.

Chapter Four

Results and Discussion

4.1: MoS_2 pellets preparation and synthesis:

4.1.1: Structural analysis:

The Molybdenum disulfide powders were purchased from an Alfa Aeser firm with a purity of the powders reaching 99.9% . The powders were then pressed under a hydraulic pressure of 75 bar to establish a pellet form. The pellets with the empirical formula MoS_2:xAs, the weight ratio (x) for As in the composite is varied in the range of 0.00 – 0.80. The X-ray diffraction (XRD) patterns for the pressed pellets before sintering is shown in Fig. 4.1.

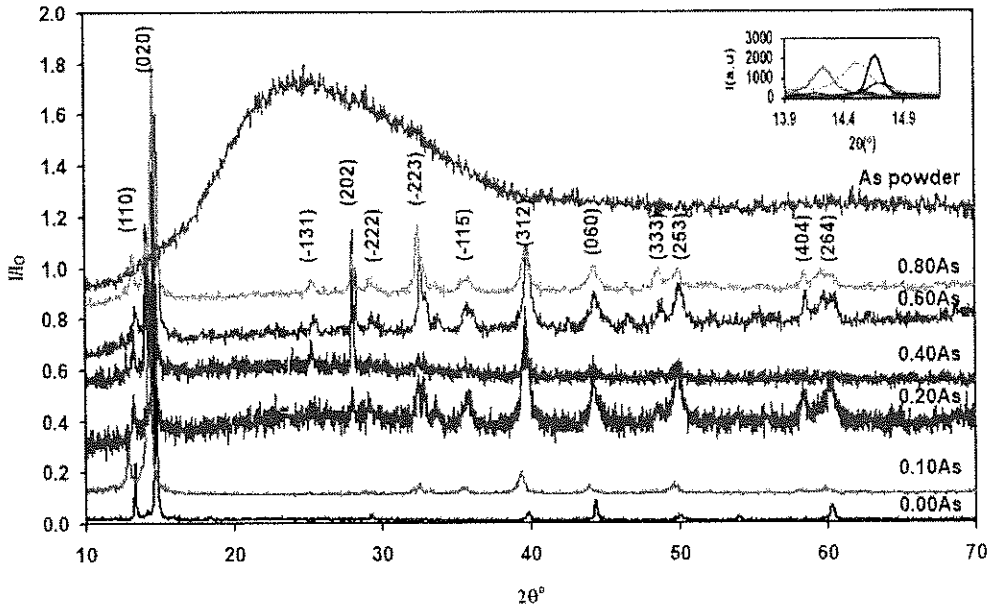

Figure 4.1: The X-ray diffraction patterns for MoS_2:xAs at 75 bar before sintering.

Deep analysis, which targeted exploring the crystalline nature of the pellets were carried out with a "TREOR 92" software packages. The software allows two options of analysis, one is simple in which client assumed to know the structure and provide lattice parameters to the system and the other assumes no structure and the client enters the observed peaks with relative intensity values and request solution assuming the particular crystal structure. For our samples, we have tried solutions including cubic, hexagonal, tetragonal, orthorhombic, monoclinic and triclinic crystal structures. The validity of each assumed solution is accepted if the difference between the observed 2θ values and the calculated ones is less than 0.001^o. All peaks refer to MoS_2 due to amorphous structure for As. The best solution that verifies this criteria was the monoclinic structure. MoS_2 are known to exhibit the hexagonal structure for this reason, we went to the belief that monoclinic structure could have resulted from the pressure effect. For this reason, we have repeated experiments by applying various hydraulic pressures to form the pellets. Particularly, we prepared samples of MoS_2 at five different hydraulic pressures (10 bar, 25 bar, 50 bar, 75 bar and 100 bar). The X-ray diffraction (XRD) patterns which resulted from these samples were also related to monoclinic structures with Lattice parameters $a = 7.78A^o$, $b = 12.21\,A^o$, $c = 13.10\,A^o$ and $\beta = 96.79^o$ for 10 bar sample. Slight variations in the lattice parameters occurred due to the pressure effect.

The maximum peak was indexed along the (020) orientation direction. These diffraction peaks are shown in the inset. of Fig. 4.1. The diffraction angles at which the maximum peak appeared is also tabulated in Table 4.1. The table also shows the lattice parameters (a, b, c) for each MoS_2:xAs sample at room temperature,

broadening width (β), crystallite size (D), strain (ε), and stacking faults percentages (SF).

Table 4.1 The structural parameters of MoS_2:xAs of main peak.

X	2Θ(°)	Lattice constant (A°)			β X10^{-3}	D (nm)	εX10^{-3}	SF%	δ(X10^{12}line/cm^2)		
		a-axis	b-axis	c-axis					a-axis	b-axis	c-axis
0. 00	14. 66	8. 50	12. 08	16. 83	6.28	16	12.21	0.17	0. 93	0. 65	0. 47
0. 10	14. 22	8. 69	12. 45	14. 73	10.82	11	21.69	0.29	2. 77	1. 94	1. 64
0. 20	14. 56	8. 34	12. 16	13. 39	10.82	10	21.18	0.29	2. 82	1. 94	1. 76
0. 40	14. 56	8. 37	12. 63	15. 65	11.51	10	22.54	0.31	3.19	2.11	1.70
0. 60	14. 70	8. 35	12. 04	16. 48	12.21	7	23.68	0.33	3. 56	2. 47	1. 80
0. 80	14. 50	8. 52	12. 21	16. 48	15.70	6	30.87	0.42	5. 85	4. 08	3. 14

A nonsystematic behavior of the lattice parameters is observed in Fig. 4.2 and table 4.1. The calculated average crystallite size (D), micro strain (ε), defect density (δ) and stacking faults (SF%)of the maximum peak for MoS_2:xAs samples are presented in Table 4.1. The doping process caused an increment of the value of the strain ($Fig4.3(b)$), stacking faults ($Fig4.3(c)$) and the value of the defect density along both of the a, b and $c-$axis($Fig4.4$). The average crystallite size decreased ($Fig4.3(a)$). Particularly, the decrease in the crystallite size due to an enormous number of bonding, it is possible to one atom in one of the presented bonds to leave its site. The defects appear if the number of broken bonds is too large. Furthermore, each atom in a bond is attracted to another atom in another bond. The interaction forces between bonds lead to the strained structure that in turn reduces the crystallite size of MoS_2:xAs. The grain boundaries change as a result of the change in crystallite size. Which possibly changes the electrical conductivity in the MoS_2 [48]. The energy stored in the grains due to increased dislocation density and this causes the

existing grains to shrink as a result of the driving force [49]. In addition, the increased dislocation density increases the trap states that act as a recombination centers in the materials [50].

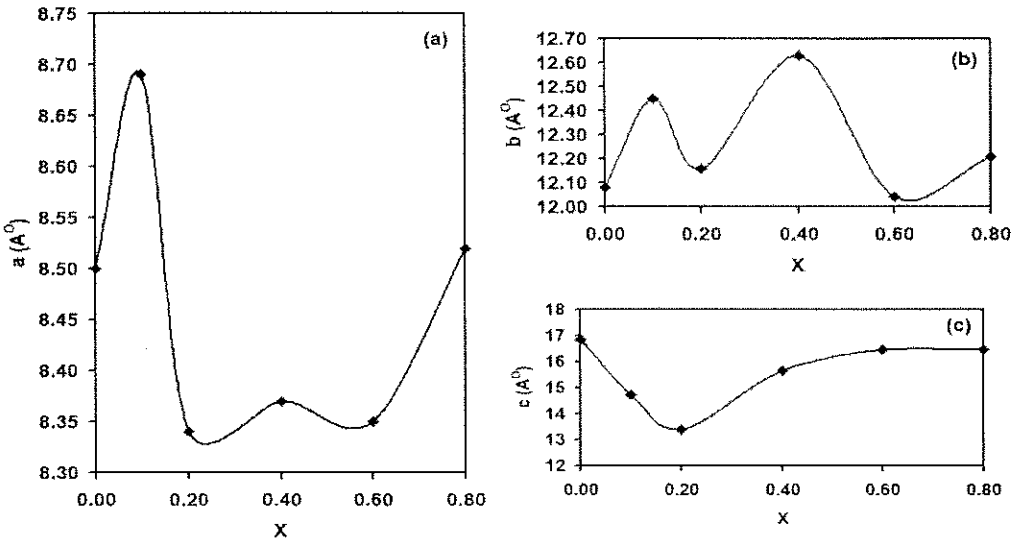

Fig. 4.2 (a), (b) and (c) The lattice parameters (a, b, c).

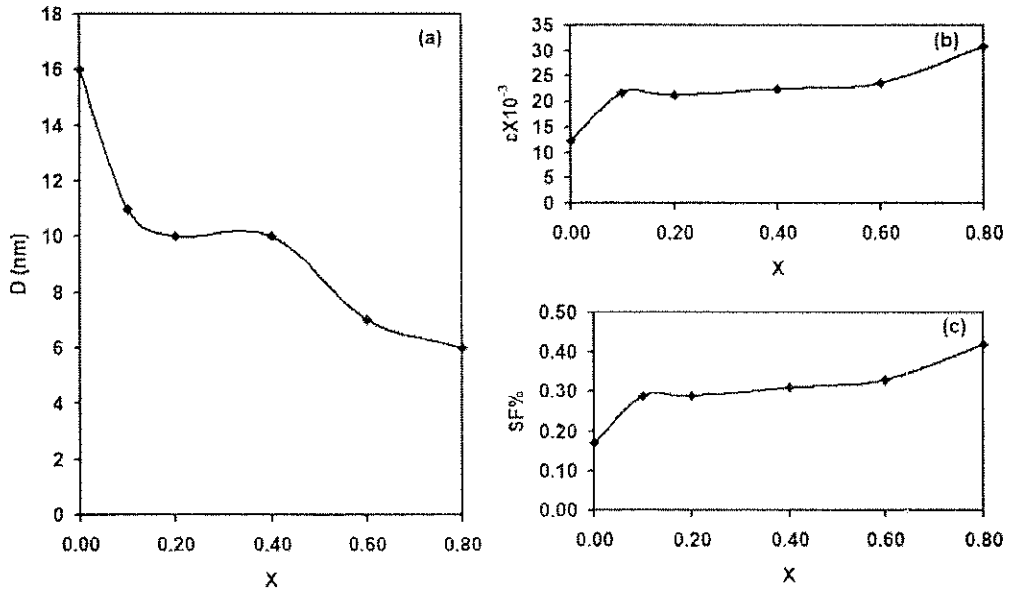

Fig. 4.3 (a), (b) and (c) Shows the average crystallite size (D), micro strain (ε) and stacking faults $(SF\%)$ from the maximum peak for MoS2: xAs samples.

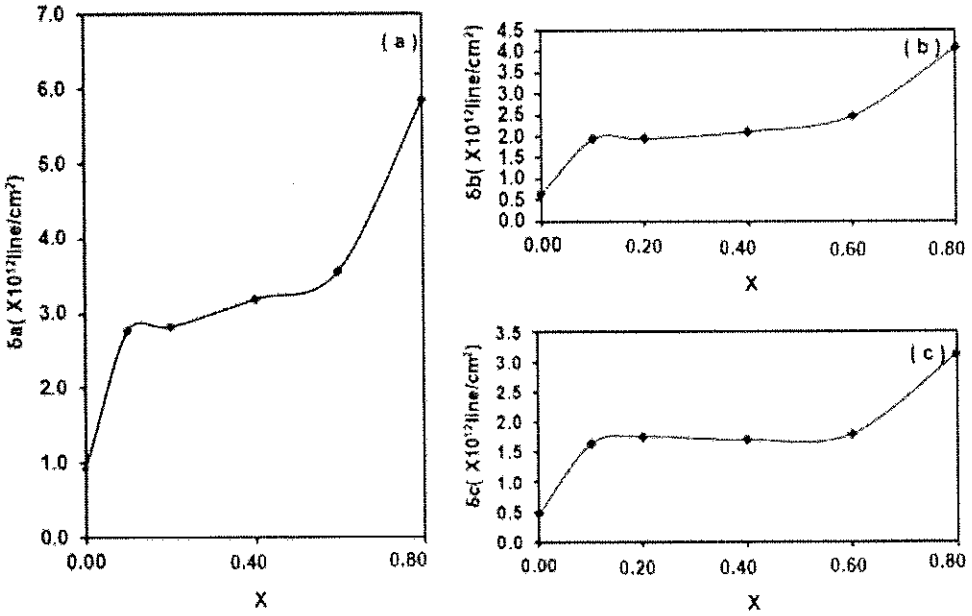

Fig. 4.4 $(a), (b)$ and (c) The defect density(δ) on both a , $b$and c –axis.

It is possible to think that there must be an interaction between arsenic (As) atoms of ionic radius of $0.58\,A^0$ [51] which is much lower than of molybdenum (Mo) $0.70\,A^0$ [52]. As MoS_2 can exhibit Mo vacancy, may be arsenic ions replace vacant sites of molybdenum forming Arsenic trisulfide (As_2S_3). MoS_2 may also contain sulfa vacancy. Then, as shown in table 4.2 comparing the ionic radius of sulfur and oxygen atoms indicate that the ionic radius of oxygen atoms which is $1.32A^0$ [53] is smaller than that of sulfur atom $1.84\ A^0$ [54], thus it can form molybdenum trioxide (MoO_3).

Table 4.2: The ionic radius and electronic configuration for MoS_2:xAs samples.

Sample	Ionic radius (Å)	Electronic configuration
Mo	0. 70 [51]	[Kr] $4d^5\ 5s^1$
S	1. 84 [53]	[Ne] $3s^2\ 3p^4$
As	0. 58 [50]	[Ar] $3d^{10}4s^24p^3$
O	1. 32 [52]	[He] $2s^2\ 2p^4$

The chemical interaction between the material composers shows an increase in the defect along a, b and c –axes. The bond length of As- S, Mo-Mo, Mo-S, S-S, As-As, listed in Table 4.3. The shortest bond length refers to As-S interaction with highest bonding energy (598.71 KJ/mol) [55]. So as we mentioned there is a great possibility for arsenic ions to replace sites of molybdenum and form Arsenic trisulfide (As_2S_3).

Table 4.3: The bond length and bond energy of the samples.

Sample	Bond length (Å)	Bond energy (KJ/mol)
As- S	2. 24 [56]	598.71 [55]
Mo-Mo	2. 07 [57]	434. 40 [60]
Mo-S	2. 41 [58]	232.60 [61]
S-S	2. 05 [59]	265. 00 [62]
As-As	2. 57 [56]	134. 20 [63]

4.1.2: Sintering effect on structural properties:

In this section we study the sintering effect on the structural properties of MoS_2:xAs pellets. The samples reported have been sintered at $200°C$ for 20 hours in air atmosphere. The X-ray diffraction (XRD) patterns which were recorded for sintered MoS_2:xAs are shown in Fig. 4.5. XRD patterns for the MoS_2:xAs pellets before sintering and after sintering at $200°C$ for 20 hours under air atmosphere were compared (Fig.4.6 –Fig.4.11). As we can see from the Fig. 4.7 , there is an enhancement in the peak appears after sintering in $x = 0.10$ sample at $\theta = 58^o$ and it is (404). In Fig.4.9, there are two peaks disappearing after sintering in $x = 0.40$ sample at $\theta = 14^o$ and $\theta = 25^o$ and they are along (101) and (-131) directions, respectively, and two peaks appear after sintering at $\theta = 58^o$ and $\theta = 60^o$and they are indexed along (404) and (264), respectively. In Fig.4.11, there are two peaks disappear after sintering in $x = 0.80$ sample at $\theta = 25^o$ and $\theta = 48^o$ and they are along (-131) and (333) directions, respectively. In Fig. 4.6, 4.8 and 4.10, there are no change in peaks before and after sintering.

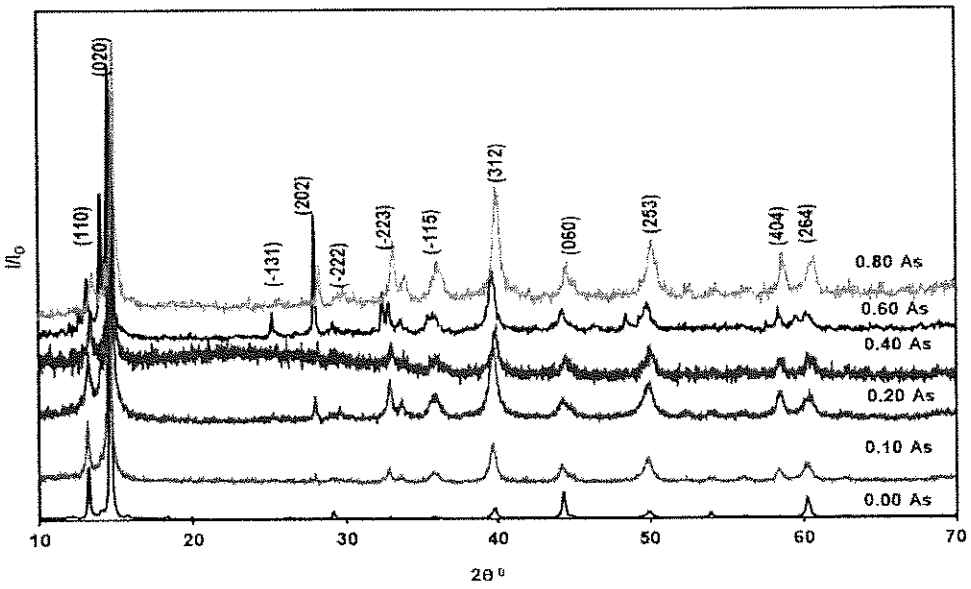

Fig. 4.5: The X-ray diffraction patterns for MoS_2:xAs pellets at 75 bar and sintering at 200 $°C$ for 20 hours.

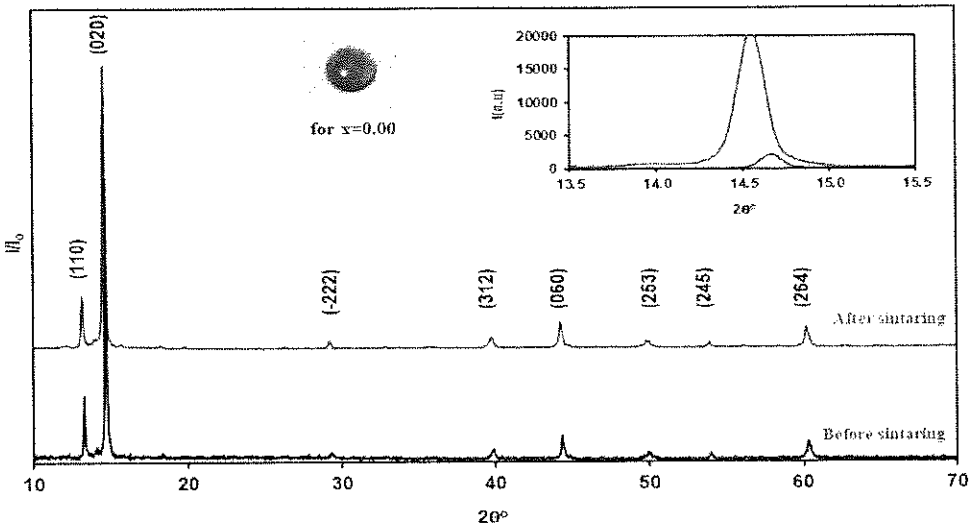

Fig. 4.6: X-ray diffraction patterns at room temperature (before sintering) and after sintering for $x = 0.00$ As sample.

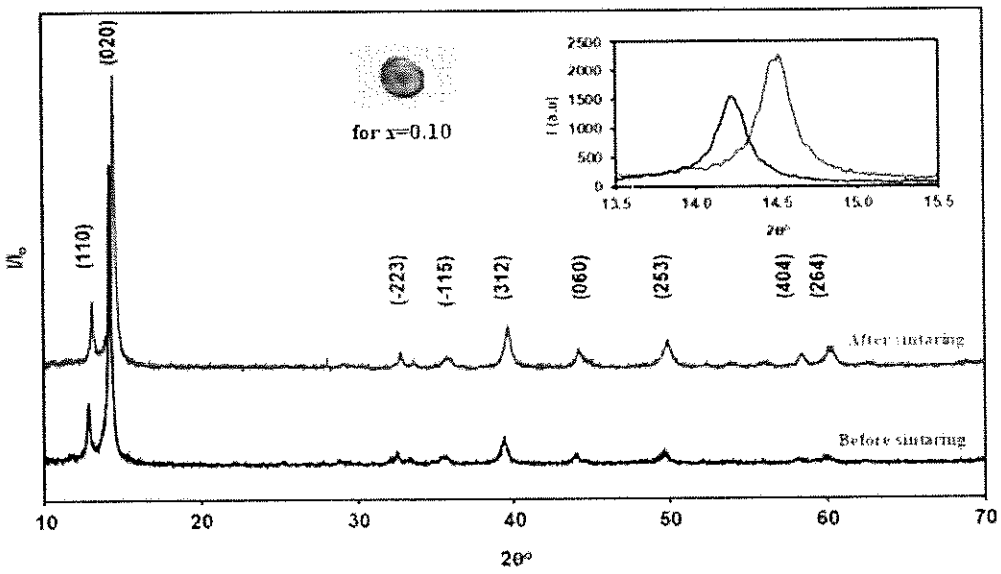

Fig. 4.7: X-ray diffraction patterns at room temperature (before sintering) and after sintering for $x = 0.10$ As sample.

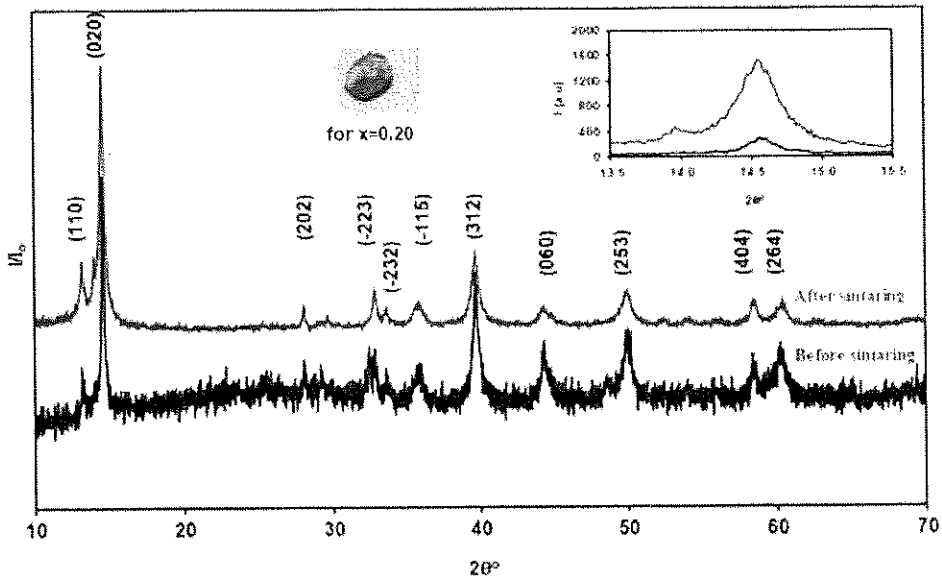

Fig. 4.8: X-ray diffraction patterns at room temperature (before sintering) and after sintering for $x = 0.20$ As sample.

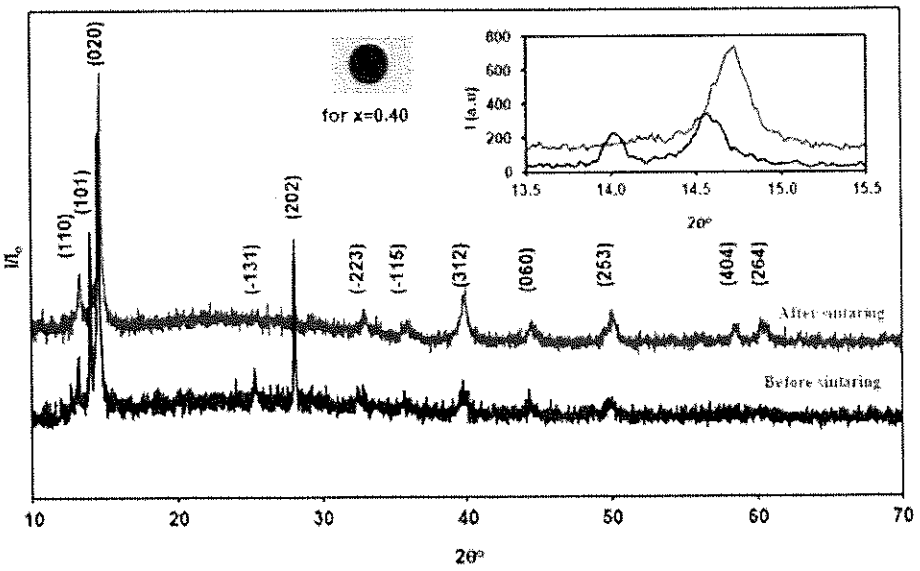

Fig. 4.9: X-ray diffraction patterns at room temperature (before sintering) and after sintering for $x = 0.40$ As sample.

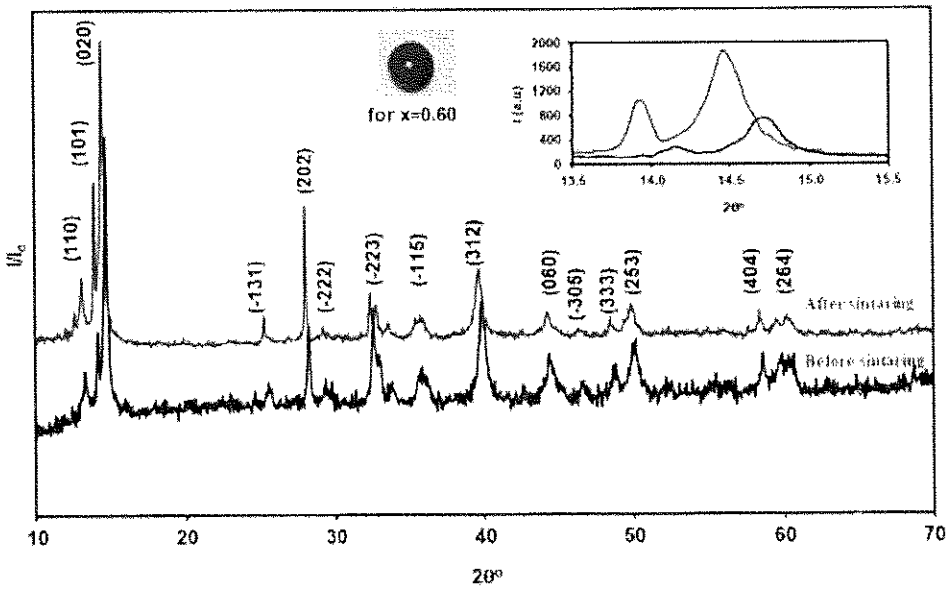

Fig. 4.10: X-ray diffraction patterns at room temperature (before sintering) and after sintering for $x = 0.60$ As sample.

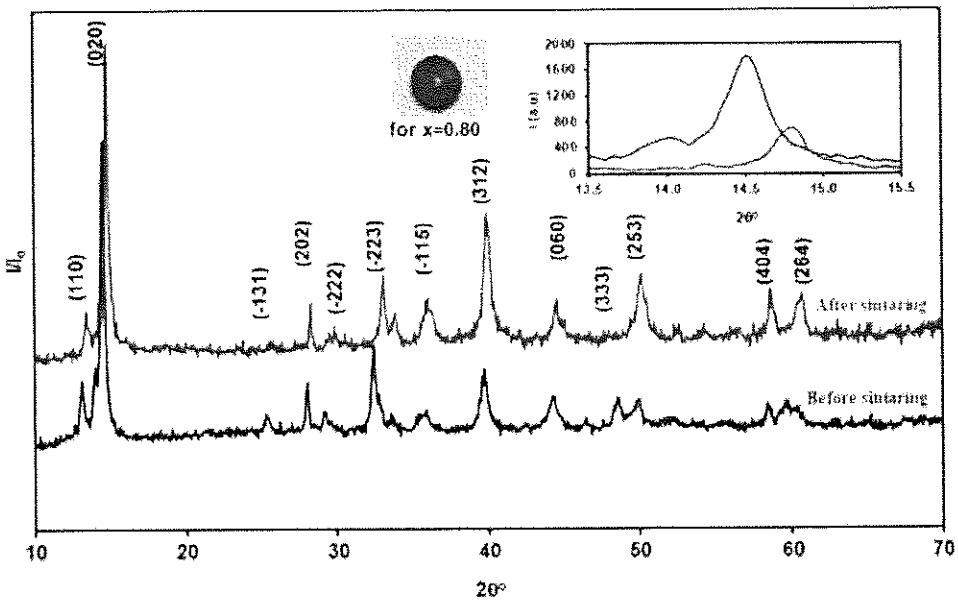

Fig. 4.11: X-ray diffraction patterns at room temperature (before sintering) and after sintering for $x = 0.80$ As sample.

The maximum peak positions for sintering process shift from $2\theta = 14.56^{o}$ to 14.80^{o}. This shift is followed by a decrease in the maximum peak intensity with increasing doping concentration. As shown in the Fig. 4.12. It is also observed that the maximum peak broadens as doping content increases. This shift to the right indicates the existence of uniform deformation in the samples.

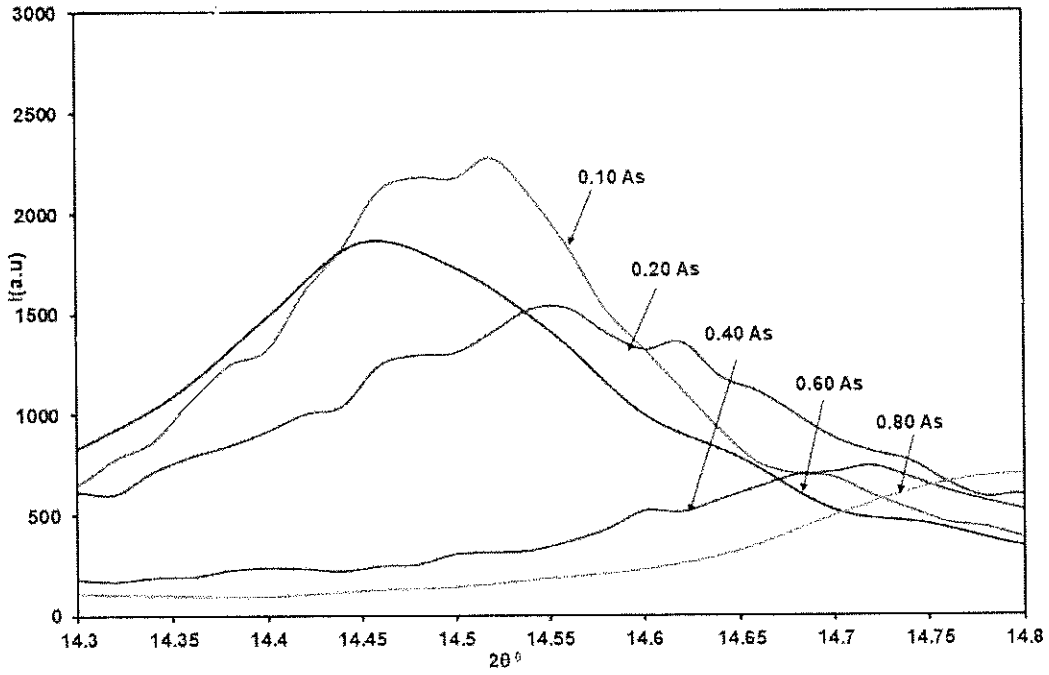

Fig. 4.12: The enlargement of the maximum peaks for MoS_2: xAs during the sintering process. it shows the variation of the maximum peak intensity with doping.

Table 4.4 The structural parameters of MoS_2: xAs sintering at $200C^o$ for 20 hours.

X	2Θ(°)	Lattice constant (A°)			β X10^{-3}	D (nm)	εX10^{-3}	SF%	δ(X10^{12}line/cm^2)		
		a-axis	b-axis	c-axis					a-axis	b-axis	c-axis
0.00	14.56	8.65	12.16	16.72	10.12	10	19.81	0.27	2.38	1.69	1.23
0.10	14.52	8.74	12.19	16.97	12.56	9	23.29	0.32	3.64	2.61	1.88
0.20	14.56	8.49	12.16	15.60	12.21	9	23.91	0.33	3.53	2.47	1.92
0.40	14.56	8.69	12.03	18.58	12.21	9	23.61	0.33	3.41	2.46	1.60
0.60	14.45	8.56	12.26	15.69	13.96	7	27.53	0.38	4.61	3.22	2.52
0.80	14.80	8.38	11.96	17.75	16.57	6	31.92	0.45	6.48	4.54	3.06

The lattice parameters are observed in Fig. 4.13 for sintering samples at $200C^o$ for 20 hours. The calculated average crystallite size (D), micro strain (ε), defect density (δ) along a, b and c −axes and stacking faults ($SF\%$) of the maximum peak for MoS_2: xAs samples after sintering at $200C^o$ for 20 hours are presented in Table 4.4. Same

increasing and decreasing trends observed for as prepared pellets are also observed for sintered pellets. The sintering process displays an increase in the value of strain ($Fig4.14(b)$), stacking faults ($Fig4.14(c)$), and the value of the defect density ($Fig4.15$) Compared to the not sintered samples. The average crystallite size ($Fig4.14(a)$), displays a decrease in its value. The prevailing belief is that there are many bonds of Arsenic trisulfide (As_2S_3) or molybdenum trioxide (MoO_3) higher than as prepared pellets.

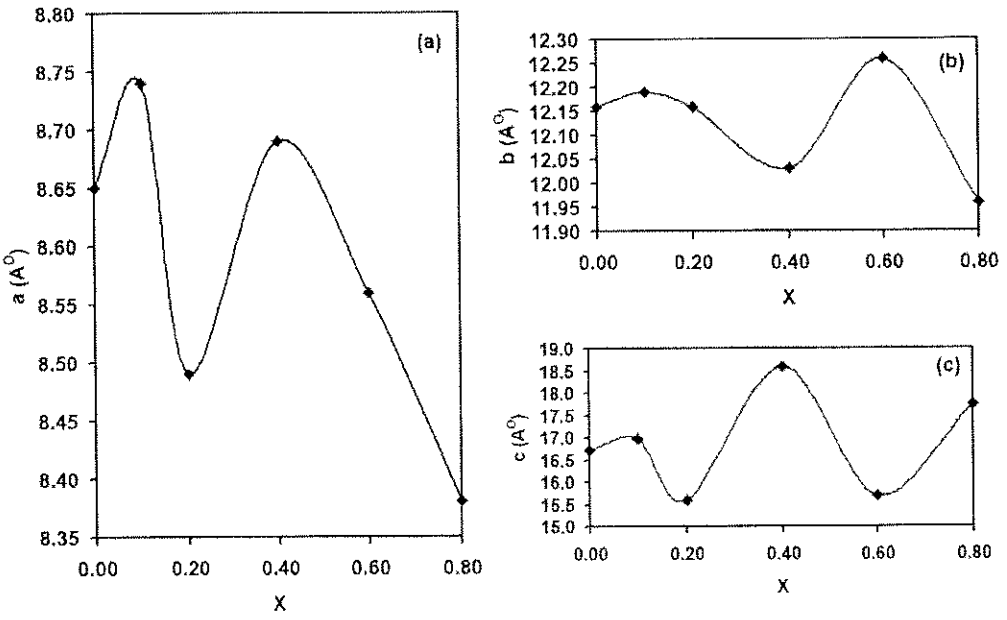

Fig. 4.13 $(a), (b)$ and (c) The lattice parameters (a, b, c) for MoS_2: xAs during the sintering process.

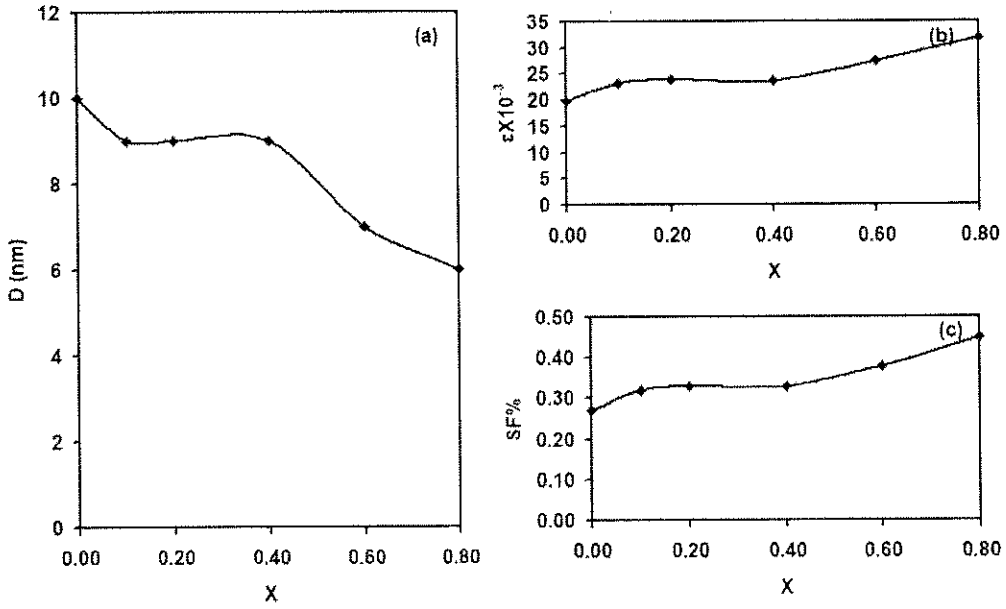

Fig. 4.14(a), (b) and (c) Shows the average crystallite size (D), micro strain (ε) and stacking faults $(SF\%)$ from the maximum peak for MoS_2: xAs samples during the sintering process.

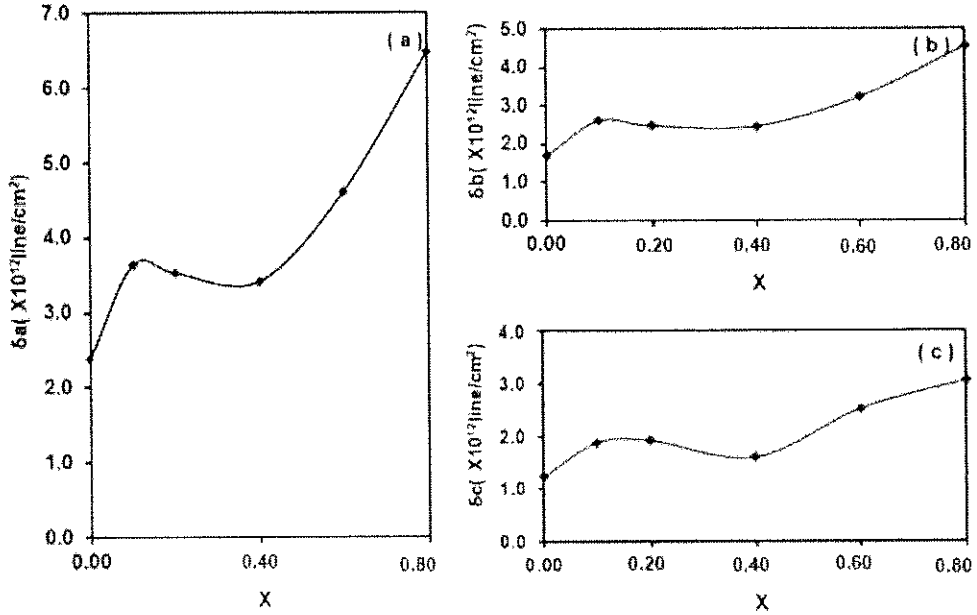

Fig. 4.15 (a), (b) and (c) The defect density(δ) on both a , band c –axis for MoS_2: xAs during the sintering process .

As a necessary work we attempted to observe the modified permanent crystallography in the samples after sintering process. The scanning electron microscopy images for an enlargement of $300, 1000, 5000$ and 10000 (for some samples) times for MoS_2: xAs samples with As weight ratio $x = 0.00,\ 0.10,\ 0.20,\ 0.40,\ 0.60$ and 0.80, are shown in figures (from Fig.4.16 to Fig.4.21). Amassing distribution of grains can be seen in these figures.

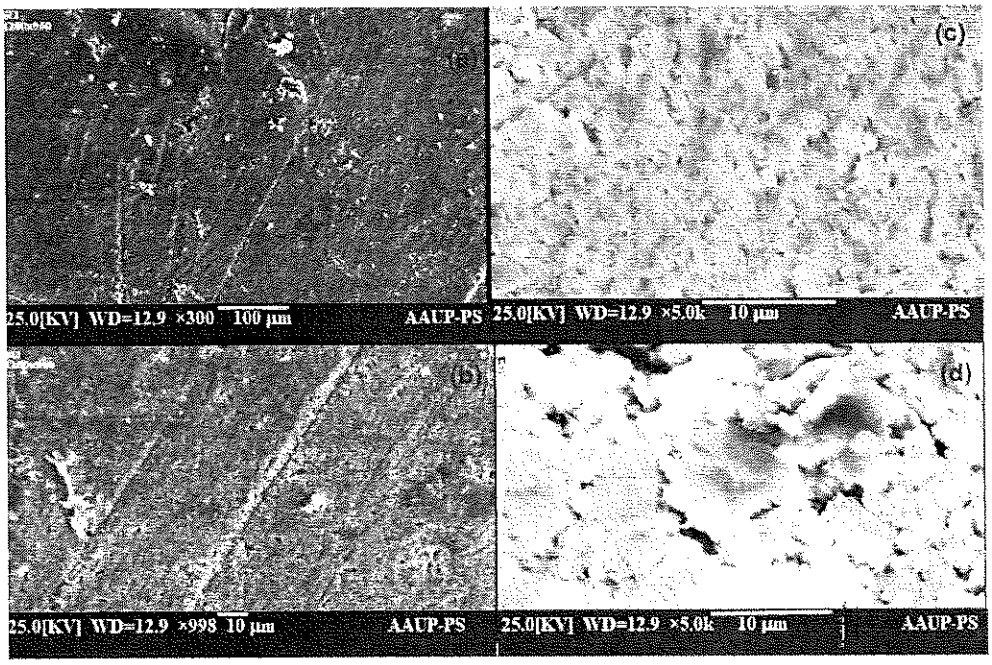

Fig. 4. 16: The SEM for $x = 0.00$ sample for an enlargements of (a) 300. (b) 1000, (c) 5000 and (d) 5000 times cross.

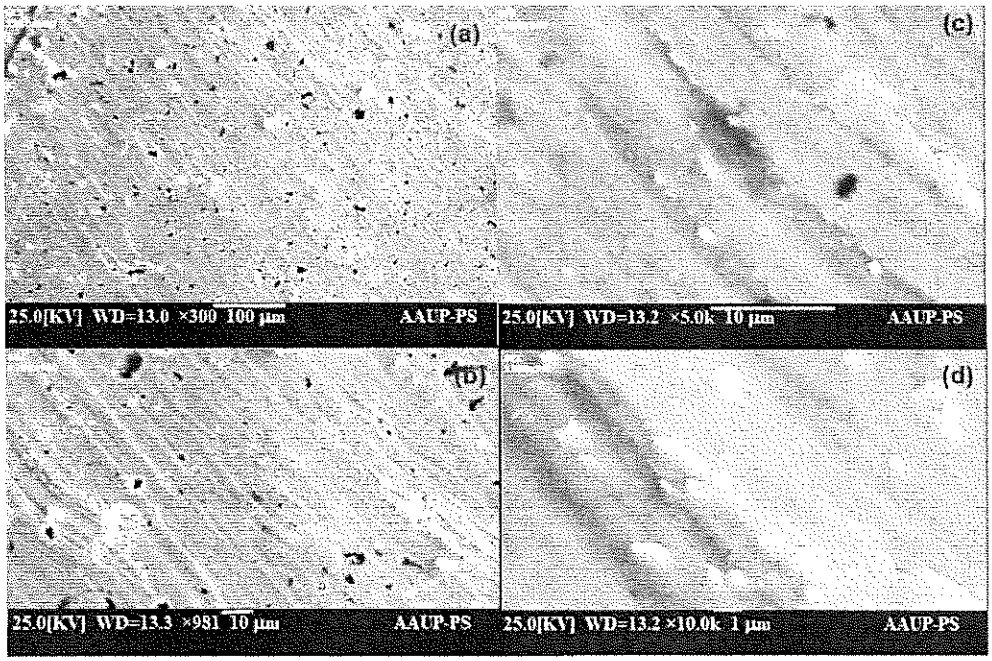

Fig. 4. 17: The SEM for $x = 0.10$ sample for an enlargements of (a) 300, (b) 1000, (c) 5000 and (d) 10000 times.

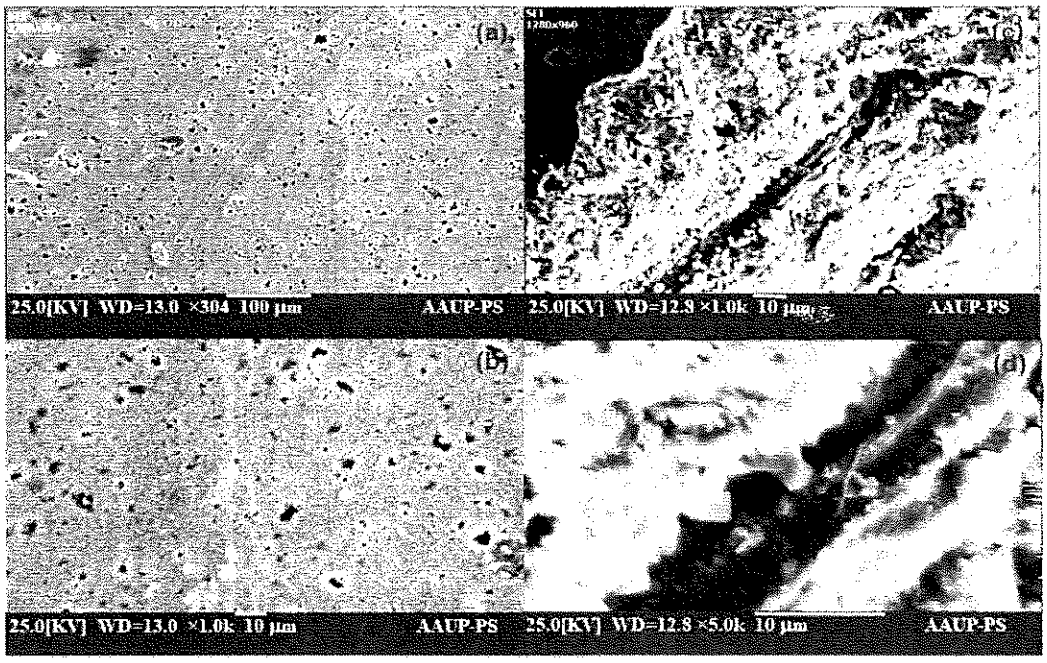

Fig. 4. 18: The SEM for $x = 0.20$ sample for an enlargements of (a) 300, (b) 1000, (c) 1000 cross (d) and 5000 times cross.

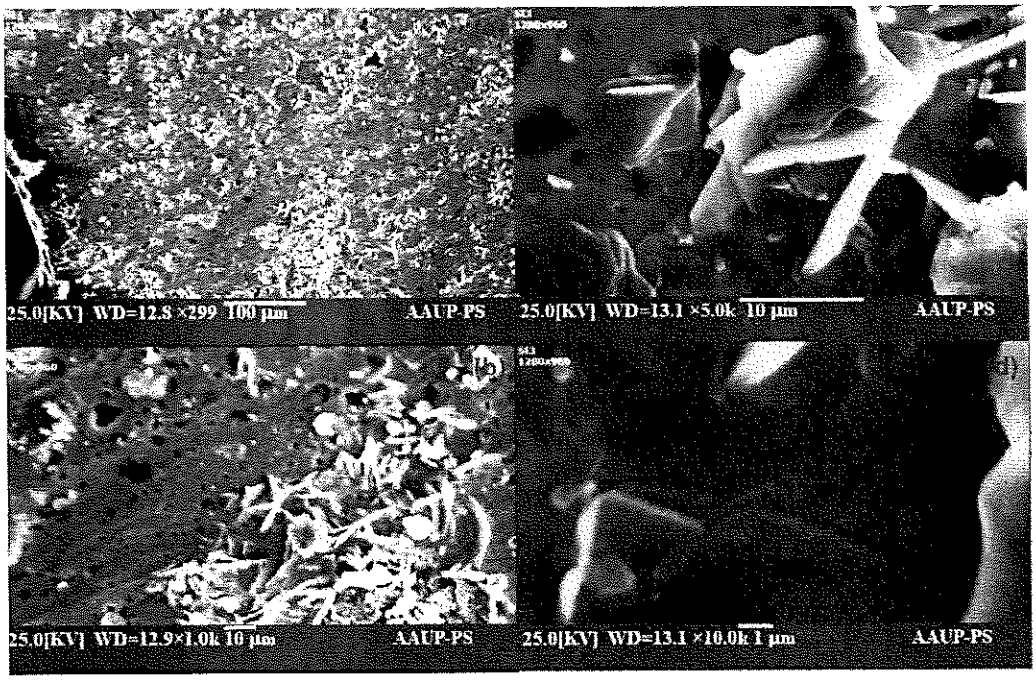

Fig. 4. 19: The SEM for $x = 0.40$ sample for an enlargements of (a) 300, (b) 1000, (c) 5000 and (d) 10000 times.

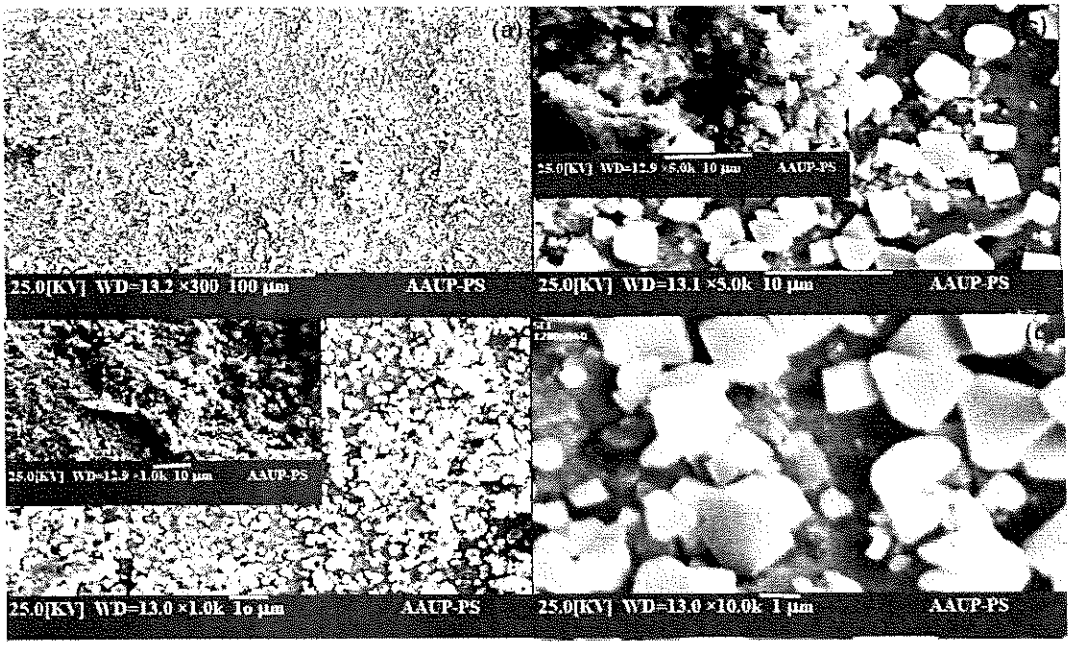

Fig. 4. 20: The SEM for $x = 0.60$ sample for an enlargements of (a) 300, (b) 1000, (c) 5000 and (d) 10000 times.

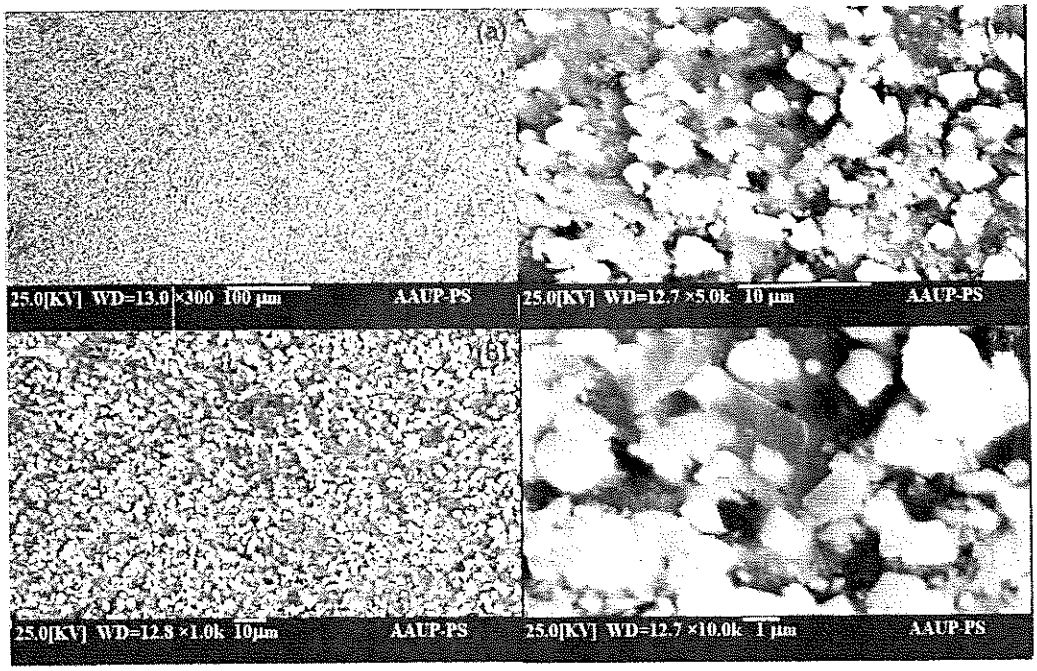

Fig. 4.21: The SEM for $x = 0.80$ sample for an enlargements of (a) 300, (b) 1000, (c) 5000 and (d) 10000 times.

It is evident from Fig. $4.16(c)$ that the surface of the undoped samples is composed of randomly distributed grains of average size of ~ 3.2 µm. Enlargement of the image by 5000 time indicate hardly observed pores in the samples. Comparing Fig. $4.16(a)$ and $4.17(a)$ are may see that the weight ratio of As at $x = 0.10$ resulted in larger degree of pores. The number of pores in the samples increased more and more with increasing x value. No distinguishable grain distribution was observed in the samples with As of weight ratio at $x = 0.20$ and $x = 0.00$. Cross-sectional view $(Fig.4.18(d))$ of the sample with As of weight ratio at 0.20 have shown that the pores and cracks also exist in the bulk of the pellets. On the other hand, samples with As of weight ratio at 0.40 displayed accumulation of flake like grains $(Fig.4.19\ (a), (b)$ and $(c))$ of average sizes of 18 µm. Samples with larger As weight ratio Fig 4.20 and Fig.4.21 displayed a

surface full of randomly distributed grains. The shape of these grains in trapezoidal and of the average sizes of 2.0 μm.

These figures show the doping process for As in MoS_2 and the appearance of grains in Fig 4.20 and Fig.4.21 indicate that the solubility limit is reached. So the formula changes from MoS2:xAs to $MoAs_xS_2$ formula. To understand the nature of the excess grains on the surface the energy dispersive x-ray (EDS) analysis were employed.

The solubility limit happened when $x = 0.40$, this means that there is no longer any effect of increasing arsenic on the MoS_2. Arsenic reacts with oxygen to produce arsenic(III) oxide (As_2O_3) $at\ x = 0.60$ and thiosulfate (S_2O_3) was formed as a result of the interaction between oxygen and sulfur at $x = 0.80$ as shown in table 4.5 , which displays atomic % of each element for $MoAs_xS_2$ samples by using Scanning electron microscopy (SEM).

Table 4.5 The atomic % for MoS_2:xAs samples.

sample	Mo at. %	S at. %	As at. %	O at. %
x=0.00	29.45	62.00	0.00	0.00
x=0.10	29.28	56.36	2.90	0.00
x=0.20	29.95	58.39	5.58	0.00
x=0.40	22.64	47.20	5.00	0.00
x=0.60	0.90	3.28	34.29	56.70
x=0.80	14.16	32.22	4.75	45.66

The energy dispersive x-ray analysis shown in table 4.5 indicate that for x values larger than 2 oxidation of As have started. It means that the solubility limit is reached at $x = 0.40$.

4.2: Electrical properties.

The electrical properties of the as prepared and sintered $MoAs_xS_2$ samples are studied here. For this purpose Ag electrical contacts were located on each side of the samples for two point measurements. The ohmocity contacts were tested for all sintered pellets, it is illustrated in Fig. 4.22 , shows the current (I) –voltage (V) plots for all sintered $MoAs_xS_2$ samples. As can be seen from the figures, all curves are linear. Although they are linear, they are not follow Ohm's law because they are semiconductors.

From the literature review, the micrometre thick films of molybdenum disulfide (MoS_2) displayed thermal response of $-600\ \mu V/K$ at a temperature difference of $40\ ^{\circ}C$, negative sign indicates that the polarity of the material is n-type [64]. This is consistent with our findings on the pure MoS_2 sample, that exhibits n-type conduction. From the literature review, we find the effect of doped MoS_2 on resistivity. Single crystals of rhenium-doped MoS_2 prepared by chemical vapor transport method, the temperature-dependent resistivity and hall coefficient were measured in the range of $20 - 300\ K$, all samples are n-type in nature with energy gap shows a red shift by increasing the doping concentrations [65]. The deposited MoS_2–Ta composite coatings with a high load-bearing capacity prepared by the pulsed-DC magnetron sputtering technique exhibited excellent fatigue resistance [66]. In our work, we find that the $x = 0.10$, $0.20\ and\ 0.40$ exhibit n-type and the $x = 0.60$ and 0.80 exhibit p-type of conduction. The formation of arsenic(III) oxide (As_2O_3) $at\ x = 0.60$ and thiosulfate (S_2O_3) $at\ x = 0.80$, so As_2O_3 and S_2O_3 exhibit p-type of conduction.

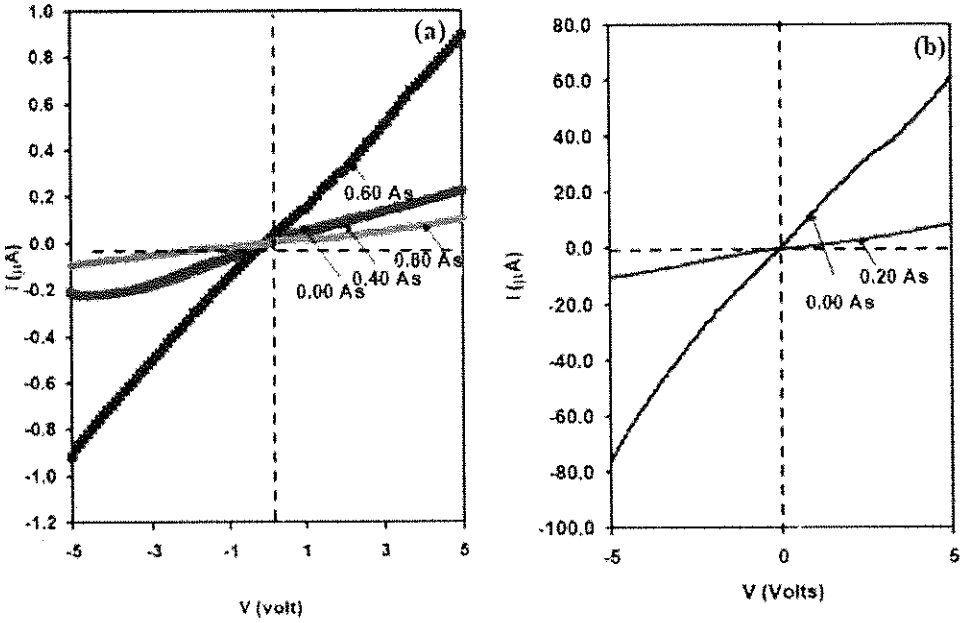

Fig. 4. 22: The $I - V$ characteristic curve for sintering $MoAs_xS_2$ samples.

Fig. 4.23 displays the resistivity of bars for sintered $MoAs_xS_2$ pellets. As can be seen from the figure, the resistivity for sintered $MoAs_xS_2$ samples of $x = 0.00, 0.01$ and 0.20 decrease with temperature increasing in the range $150 - 300$ K. This confirms the semiconducting behavior of $MoAs_xS_2$ compound.

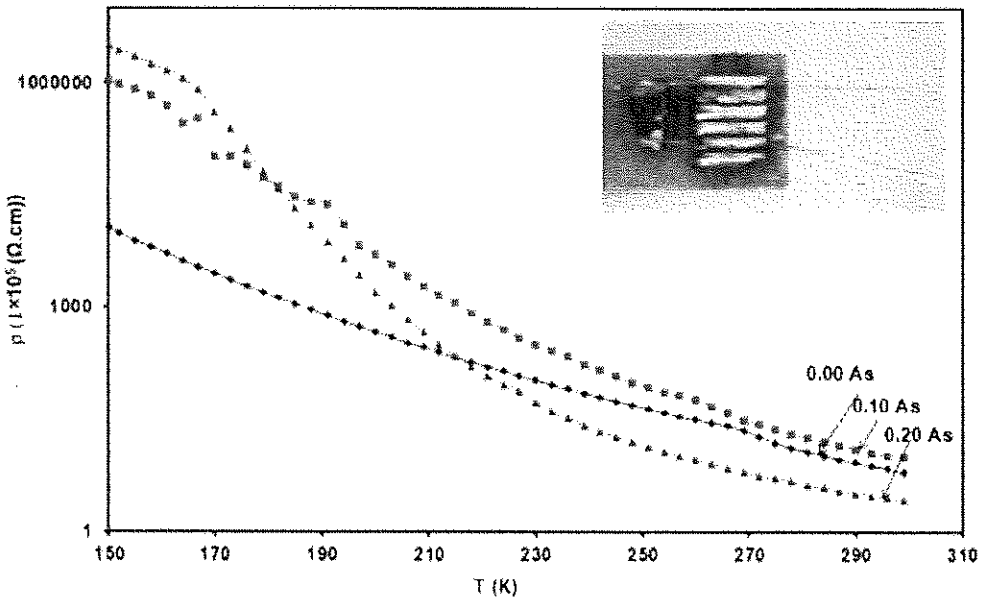

Fig. 4. 23: The resistivity versus temperature of $MoAs_xS_2$ samples.

To explore the As doping effect on the electrical properties of MoS_2, so we sampled $x = 0.00, 0.01$ and 0.20 to study the doping effect on resistivity before reaching solubility limit. The temperature (T) dependent electrical resistivity is studied in the temperature range of $(150 - 300\,\mathrm{K})$ in a closed cycle the cryostat. The semilogerethmic scale of the electrical resistivity as a function of temperature is shown in Fig. 4.23. It is evident from the figure that the electrical resistivity decrease with increasing temperature with different trends of variation that depends on the doping level. To understand the nature of conduction, the equation $(\rho = \rho_0\, exp\, (E_\sigma/KT))$ is employed. Where E_σ is the activation energy and ρ_0 is the pre exponential factor. Fig. 4.24 displays $ln\rho - T^{-1}$ variation for $MoAs_xS_2$ doped with As of content of $x = 0.00,\ 0.10$ and 0.20 . As can be seen from the figure, the activation energy is obtained from the slope of variation. Regions of constant activation energy means domination of one conduction mechanism. While varying Ea with T means more than

one conduction mechanism is contributing. For our samples we have assumed the domination of thermionic emission and variable range hopping at the same time. Calculations which proofs the presence of conduction by thermionic emission estimated from the $ln\rho - T^{-1}$ plots displayed in Fig. 4.24. In accordance with the linear slops the activation energy values which are shown in table 4.6 are increasing with increasing doping content. It means that MoS_2 exhibit extrinsic nature of conduction with deeper (donor) levels as As content increases. If the condition for the validity of hopping conduction presented by $T_o > 10^3, \gamma R > 1$ is satisfied, so the hopping transport mechanism dominates and the evaluation of the Mott's variable range hopping parameters becomes straight forward. Plotting of $ln(\rho) - T^{-\frac{1}{4}}$ (shown in Fig.4.25), then it is possible to determine the value of T_o (electronic state of disorder) using the slope of the solid line (Fig.4.25), the Mott's variable range hopping parameters for $MoAs_xS_2$ pellets have determined in table 4.6, we find $N(E_F)$ using the relation ($T_0 = \frac{\lambda\gamma^3}{K_B N(E_F)}$) mentioned in section 2.3.2, the average hopping distance (R) and the average hopping energy (W) are given by the relations ($R = \left(\frac{9}{8\pi\gamma K_B T N(E_F)}\right)^{\frac{1}{4}}$) and ($W = \frac{3}{4\pi R^3 N(E_F)}$), respectively. The parameters are evaluated for a localization length of 5 Å in temperature range $150 - 300$ K. The calculated of hopping parameter values assuming the validity of the equation ($\rho_{hp}(T) = \rho^2 \, exp\,(-\left(\frac{T0}{T}\right))^{-1/4}$), which indicates the validity of the hopping transport in the our region.

The variation of the activation energy with temperature can be easily recognized by ($\sigma_{th} = \sigma_o \, exp\,(-E\sigma/KT)$), we then have the following equation: ($dE\sigma\,(T) =$

$-\frac{d\ ln\ (\sigma)-d\ ln\ (\sigma 0)}{d(kT)^{-1}}$). Such behavior is clearly shown in the Fig. 4.26, however, as the statistical Fermi level shifts with temperature, the value of Eσ changes over wide temperature ranges. The existence of $E\sigma$ indicates that the impurities, broken bonds or material inhomogeneities reserve particular location in the energy band gap [47].

Table 4.6. The evaluated electrical parameters for $MoAs_xS_2$ samples.

	E_σ (meV)	γ(cm^{-1})×10^7	To(K)×10^8	N(E_F)(cm^3/eV) ×10^{19}	R(200K)(cm)×10^{-7}	W(200)(meV)	γR
x=0. 00	194. 93	2. 00	7. 23	24.05	4.49	109.69	8.98
x=0. 10	327. 75	2. 00	58. 89	2.95	36.67	1.64	73.34
x=0. 20	442. 46	2. 00	138. 42	1.25	86.54	0.29	173.08

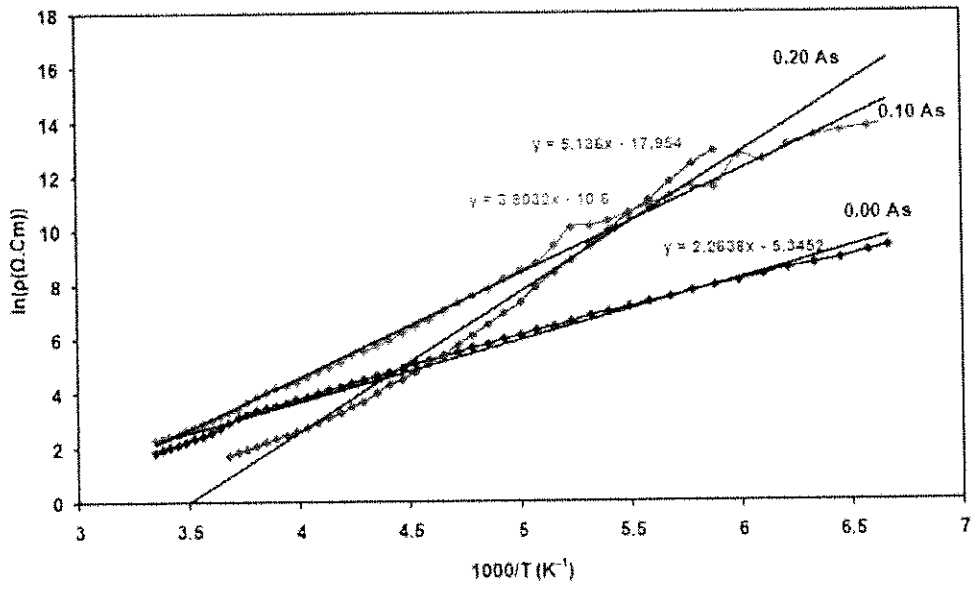

Fig. 4.24: The $ln\ \rho$ versus $1000/T$ of $MoAs_xS_2$ samples.

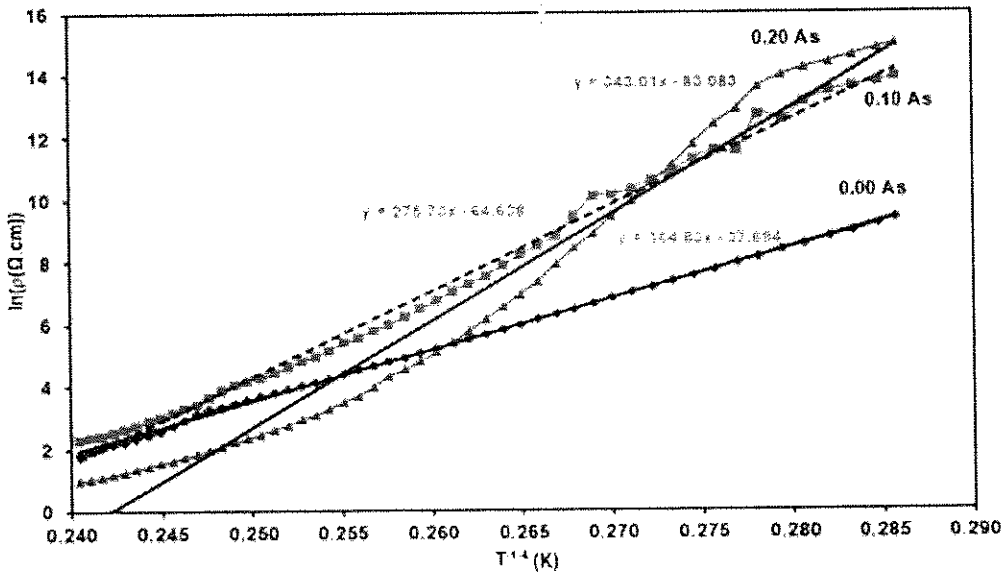

Fig. 4.25: The $ln\,\rho$ versus $T^{-\frac{1}{4}}$ of $MoAs_xS_2$ samples.

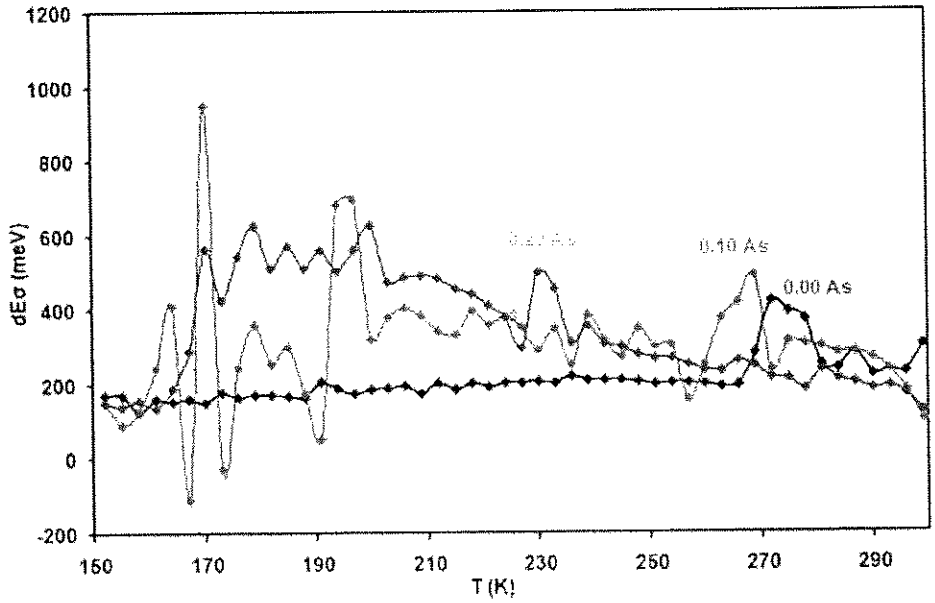

Fig. 4.26: The $dE_\sigma - T$ dependence for $MoAs_xS_2$ samples.

4. 3: Impedance spectroscopy analyses

To reveal the AC electrical properties of the sintered $MoAs_xS_2$ samples, the impedance spectroscopy technique was investigated using Agilent $4291B\ RF$ Signal Generator/impedance analyzer in the frequency range of $10 - 1800\ MHz$. The capacitance (C), impedance (Z) and conductance (G) spectra are investigated as a function of frequency (f) for the sintered $MoAs_xS_2$.

Fig. 4.27 represents the capacitance of $MoAs_xS_2$ with $x = 0.00, 0.01$ and 0.20 we sampled $x = 0.00, 0.01$ and 0.20 to study the doping effect on capacitance before reaching solubility limit.As seen from the figure, the capacitance decreases with an increase in the Ac-frequency in $x = 0.00$ and 0.10, obeying a power law of the frequency. This variation necessarily gives an electric resistance component at the interfaces [67], each sample is treated as resistance-inductance-capacitance RLC circuit connected in series. For these samples the conductivity data is illustrated in table 4.7 , the dielectric constant, dielectric dissipation factor, resistance and capacitance were found by our device (impedance analyzer) and cut off frequency f_{CO} was found by the relation ($(f_{CO} = 1/2CR\pi)$. It is clear from the Fig. 4. 27 that the As doping of $x = 0.10$ did not alter the capacitance values while increasing the doping level to $x = 0.20$ show a remarkable decrease in comparison to others in the capacitance value in the frequency domain of $0.01 - 1.60\ GHz$. For larger values the peak in C appeared indicating satisfaction of resonance condition. Resonance in spectra means more energy can be stored in the system [68].

Table 4.7. The conductivity data for $MoAs_xS_2$ samples.

		Dielectric constant	Dielectric dissipation factor	$R(\Omega)$	$C(PF)$	$f_{CO}\times10^6$ (GHz)
$f = 100Hz$	x=0.00	3.35	0.18	94.34	3.37	0.50
	x=0.10	3.09	0.10	50.87	3.08	1.02
	x=0.20	2.33	0.02	4.04	0.54	73.42
$f = 1.0GHz$	x=0.00	2.48	0.08	5.28	2.55	11.80
	x=0.10	2.50	0.03	1.90	2.57	32.65
	x=0.20	2.30	0.01	4.14	0.56	68.88
$f = 1.7GHz$	x=0.00	1.24	-0.18	-10.99	1.51	-9.58
	x=0.10	1.22	-0.13	-8.49	1.46	-12.81
	x=0.20	1.20	-0.01	0.73	2.82	77.69

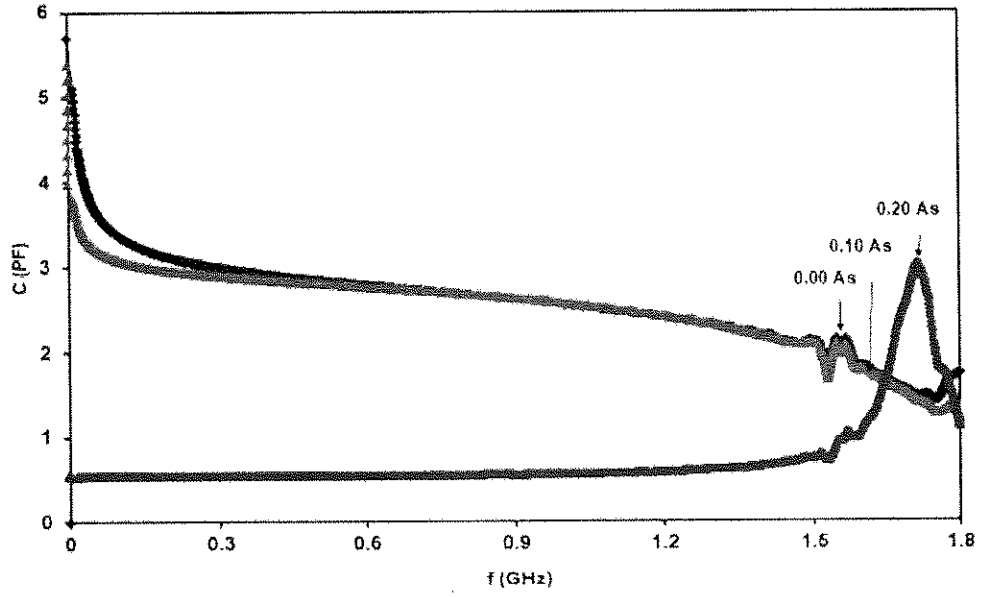

Fig. 4.27: The capacitance versus frequency for $MoAs_xS_2$ samples.

The conductance spectra for the $MoAs_xS_2$ under study are shown in Fig. 4.28. As seen from the figure, $MoAs_xS_2$ with $x = 0.00$, 0.10 and 0.20 exhibit similar trends of variation in the frequency domain of $0.01 - 1.40\,GHz$, we sampled $x = 0.00, 0.01$ and 0.20 to study the doping effect on conductance before reaching

solubility limit. $MoAs_xS_2$ started with negative values and decreased with increasing frequency. The $x = 0.00$ sample started negative at $1.60\ GHz$, $x = 0.10$ started it at $1.5\ GHz$ and $x = 0.20$ at $1.7\ GHz$ sample The explanation for the existence of the phenomenon of negative conductivity originates from traps states effects. Large density of deep-states within a narrow energy range can result in this negative conductance effect [69].

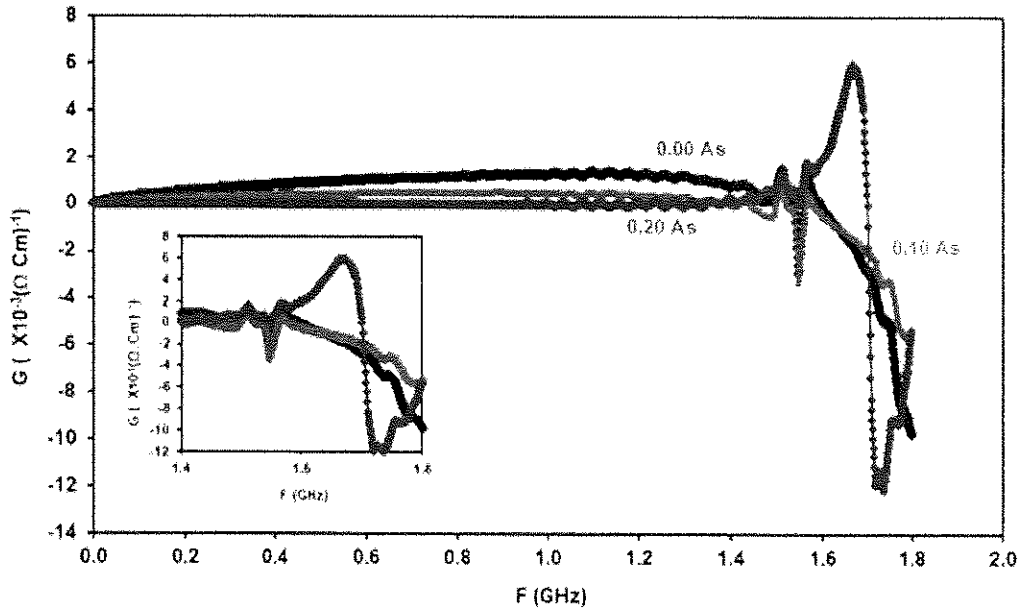

Fig. 4. 28: The conductance versus frequency for $MoAs_xS_2$ samples.

The trends of variation for frequency dependent conductivity indicate more than one transport mechanism in the pellets under this study. The alternating current (AC) conductivity spectra referred to the quantum mechanical tunneling (QMT) and/or correlated barrier hopping conduction (CBH). The $MoAs_xS_2$ conductivity spectra was modeled in accordance with the model described in sec. 2.2.3. Fig. 4.29 represent the modeled curve for pure MoS_2 pellets $\left(Fig.4.29(a)\right)$ and doped MoS_2 pellets at $x = 0.10$ $\left(Fig.4.29(b)\right)$. As seen from the figure, the conductivity of pure MoS_2 starts to

increase following an exponent power (s) value of change $\sigma = A\omega^s$ in the range of frequency $0.00 - 0.30\ GHz$, if s decrease with increasing frequency, the quantum mechanical tunneling (QMT) is dominant. The correlated barrier hopping (CBH) is dominant when the frequency exceeds $0.30GHz$, that's mean at the grain boundaries the charge carrier hops from a site to site over the potential barrier [70]. The conductivity of doped MoS_2 refers to the quantum mechanical tunneling (QMT) and correlated barrier hopping conduction (CBH) together, are demonstrated in Fig. 4.29.

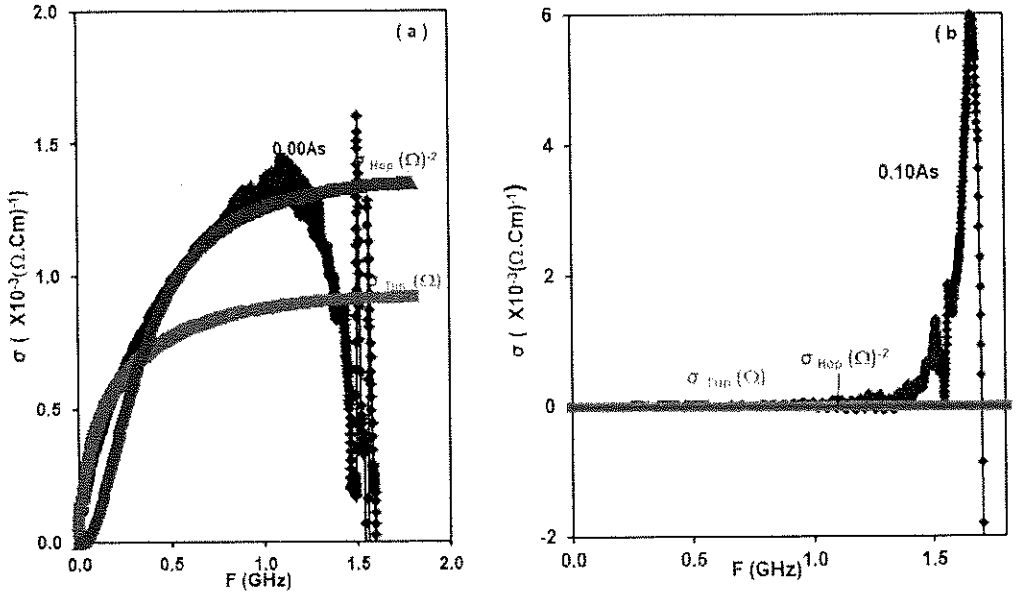

Fig. 4.29 (a, b): The modeled curve of the conductance for $MoAs_xS_2$ samples at $x = 0.00$ and 0.20, respectively.

When referring to the tabulated data in table 4.8, the doping on MoS_2 alters the hopping time constant, a decrease of τ_{hop} by 3 times is observed. The doping affect the density of localized states near Fermi level, the table shows a decrease of $N\ (E_f)$ by 25 times. The fitting parameters are also shown in table 4.8.

4.8: Ac conduction parameters for $MoAs_xS_2$ samples at $x = 0.00$ and 0.20.

parameter	x=0.00	x=0.20
τ_0 (ns)	10.00	10.00
τ_{hop} (ns)	3.00	1.00
$N(E_F)$ ($x10^{18}$ $cm^{-3}eV$)	25.00	1.00
$\sigma(L)$ x (10^{-4} $\Omega^{-1}cm^{-1}$)	0.01	0.01
$\sigma(H)$ x (10^{-6} $\Omega^{-1}cm^{-1}$)	1400.00	100.00

It is noted from Fig. 4. 30 , the impedance spectra for the $MoAs_xS_2$ under study are with $x = 0.00,\ 0.10$ and 0.20, i is noted that a values decreases by more than one order of magnitude within a narrow range of frequency $0.01 - 0.30\ GHz$. The higher the impedance are $14.93\ X10^3\Omega$, $30.84\ X10^3\Omega$ and $31.47\ X10^4\Omega$ for $x = 0.00, 0.10$ and 0.20 , respectively, and the lower the impedance values are 47.55Ω, 49.02Ω and 30.58Ω for $x = 0.00, 0.10$ and 0.20 , respectively. This behavior indicated a larger delaminated areas within the substrate due to corrosion. The impedance relies heavily on the resistance and capacitance values for that reason it shows minor and major peaks very similar to these for capacitance and conductance [71].

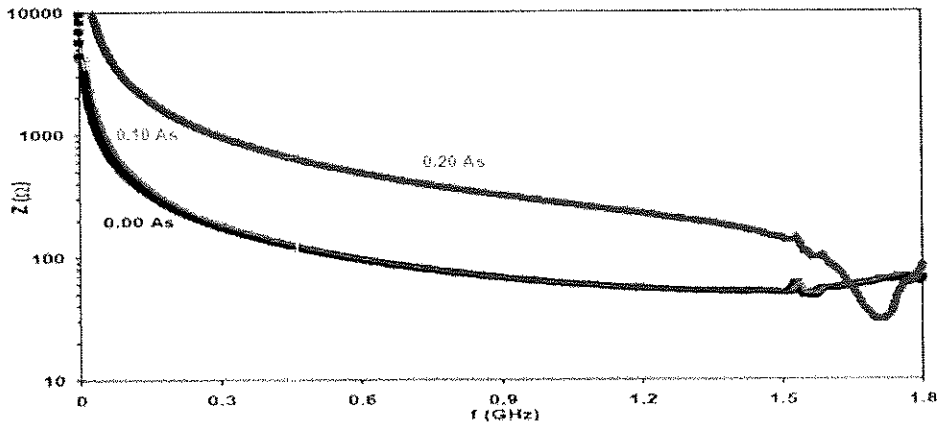

Fig. 4. 30: The impedance versus frequency for $MoAs_xS_2$ samples.

Chapter five

Conclusions

In this study, we attempted to alter the structural and electrical properties of molybdenum sulfide by doping them with arsenic. It is observed that As atoms occupy interstitial positions in the vacant sites of Mo forcing a change in the interaction from Mo-S to As-S. The increased content of AS-S bonds in the structure of MoS_2 exceeds the solubility limit for arsenic content of 0.40 in the samples. All the structural parameters including the crystallite sizes and defect density are negatively affected by the As doping. In addition, a remarkable increase in the electrical resistivity associated with increased resistivity activation energy resulted from the increased doping content in the samples. Deep analysis of the electrical parameters have shown the domination of minded type of dc conduction. Particularly, current conduction by thermionic emission and by variable range hopping dominated the conduction in the sample. Moreover, the conductivity spectral analysis have shown that the Ac conductivity is limited by the quantum mechanical tunneling and by the correlated barrier hopping of charge particles at the grain boundaries in response to Ac signal frequency. However, interesting feature presented by deceased values of capacitance and negative conductance are detected for the As doped MoS_2 powders. These features are promising as they necessarily indicate the suitability of the powder pellets for microwave based communication technology.

References

[1] Alarifi, Ibrahim M., Youssef O. Al-Ghamdi, Reem Darwesh, Mohammad Omaish Ansari, and Mohammad Kashif Uddin. "Properties and application of MoS2 nanopowder: Characterization, Congo red dye adsorption, and optimization." *journal of materials research and technology* 13 (2021): 1169-1180.

[2] Ishag, Alhadi, and Yubing Sun. "Recent Advances in Two-Dimensional MoS2 Nanosheets for Environmental Application." *Industrial & Engineering Chemistry Research* 60, no. 22 (2021): 8007-8026..

[3] Kristy, A. Periyanayaga, S. Harish, M. Omprakash, K. D. Nisha, H. Ikeda, and M. Navaneethan. "Interface effect of graphene oxide in MoS2 layered nanosheets for thermoelectric application." *Journal of Materials Science: Materials in Electronics* 33, no. 11 (2022): 8711-8723.

[4] Mutalik, Chinmaya, Dyah Ika Krisnawati, Shivaraj B. Patil, Muhamad Khafid, Didik Susetiyanto Atmojo, Puguh Santoso, Ssu-Chiao Lu, Di-Yan Wang, and Tsung-Rong Kuo. "Phase-dependent MoS2 nanoflowers for light-driven antibacterial application." *ACS Sustainable Chemistry & Engineering* 9, no. 23 (2021): 7904-7912.

[5] Wang, Yuan, Bihong Zhang, Yun Tang, Faqiong Zhao, and Baizhao Zeng. "Fabrication and application of a rutin electrochemical sensor based on rose-like AuNPs-MoS2-GN composite and molecularly imprinted chitosan." *Microchemical Journal* 168 (2021): 106505.

[6] Zhou, Qunfei, Zhen-Fei Liu, Tobin J. Marks, and Pierre Darancet. "Range-separated hybrid functionals for mixed dimensional heterojunctions: Application to phthalocyanines/MoS2." *APL Materials* 9, no. 12 (2021): 121112.

[7] Gopalakrishnan, Arthi, Lignesh Durai, Jiaojiao Ma, Chang Yi Kong, and Sushmee Badhulika. "Vertically aligned few-layer crumpled MoS2 hybrid nanostructure on porous Ni foam toward promising binder-free methanol electro-oxidation application." *Energy & Fuels* 35, no. 12 (2021): 10169-10180.

[8] Karmakar, Srikanta, Rajat Sarkar, Chandra Sekhar Tiwary, and Pathik Kumbhakar. "Synthesis of bilayer MoS2 nanosheets by green chemistry approach and its application in triboelectric and catalytic energy harvesting." *Journal of Alloys and Compounds* 844 (2020): 155690.

[9] Liu, Lixuan, Kun Ye, Zhipeng Yu, Zhiyan Jia, Jianyong Xiang, Anmin Nie, Fusheng Wen et al. "Photodetection application of one-step synthesized wafer-scale monolayer MoS2 by chemical vapor deposition." *2D Materials* 7, no. 2 (2020): 025020.

[10] Kumar, Sujit, Anjali Sharma, Yen Teng Ho, Akhilesh Pandey, Monika Tomar, A. K. Kapoor, Edward Yi Chang, and Vinay Gupta. "High performance UV photodetector based on MoS2 layers grown by pulsed laser deposition technique." *Journal of Alloys and Compounds* 835 (2020): 155222.

[11] Wang, Jiayu, Jiahao Deng, Yunbo Li, Huan Yuan, and Ming Xu. "ZnO nanocrystal-coated MoS2 nanosheets with enhanced ultraviolet light gas sensitive activity studied by surface photovoltage technique." *Ceramics International* 46, no. 8 (2020): 11427-11431.

[12] Chandrabose, Gauthaman, Avishek Dey, Shivani Singh Gaur, Sudhagar Pitchaimuthu, Hema Jagadeesan, N. St John Braithwaite, Vimalnath Selvaraj, Vasant Kumar, and Satheesh Krishnamurthy. "Removal and degradation of mixed dye

pollutants by integrated adsorption-photocatalysis technique using 2-D MoS2/TiO2 nanocomposite." *Chemosphere* 279 (2021): 130467.

[13] Das, Akash, and Manik Pradhan. "Investigation of the optical beam shifts for monolayer MoS2 using polarimetric technique." *Journal of Optics* 22, no. 10 (2020): 105004.

[14] Sridevi, R., Pravin, J. C., Babu, A. R., & Nirmal, D. (2022). Investigation of quantum confinement effects on molybdenum disulfide (mos2) based transistor using ritz galerkin finite element technique. *Silicon*, *14*(5), 2157-2163.

[15] Yehia, Hossam M., A. Abu-Oqail, Maher A. Elmaghraby, and Omayma A. Elkady. "Microstructure, hardness, and tribology properties of the (Cu/MoS2)/graphene nanocomposite via the electroless deposition and powder metallurgy technique." *Journal of Composite Materials* 54, no. 23 (2020): 3435-3446.

[16] Mirershadi, Soghra, Farhad Sattari, Afshin Alipour, and Seyedeh Zahra Mortazavi. "Non-linear thermo-optical properties of MoS2 nanoflakes by means of the Z-scan technique." *Frontiers in Physics* 8 (2020): 96.

[17] Chaudhary, Nahid, Arun Kumar, Suhaib Imtiyaz, and Manika Khanuja. "Architectural design of electrode material for supercapacitor application based on a MoS2/CeO2 heterostructure synthesized by facile hydrothermal technique." *ECS Journal of Solid State Science and Technology* 10, no. 5 (2021): 053005.

[18] Yang, Yujue, Zihao Liu, Kaixiang Shu, Ling Li, and Jingbo Li. "Improved performances of CVD-grown MoS2 based phototransistors enabled by encapsulation." *Advanced Materials Interfaces* 8, no. 11 (2021): 2100164.

[19] Xu, Hanwen, Jiawei Zhu, Qianli Ma, Jingjing Ma, Huawei Bai, Lei Chen, and Shichun Mu. "Two-dimensional MoS2: Structural properties, synthesis methods, and regulation strategies toward oxygen reduction." *Micromachines* 12, no. 3 (2021): 240.

[20] Liu, Jinkun, Zirui Jia, Wenhui Zhou, Xuehua Liu, Chuanhui Zhang, Binghui Xu, and Guanglei Wu. "Self-assembled MoS2/magnetic ferrite CuFe2O4 nanocomposite for high-efficiency microwave absorption." *Chemical Engineering Journal* 429 (2022): 132253.

[21] Jlidi, Zaineb, Sabrine Baachaoui, Noureddine Raouafi, and Said Ridene. "Temperature effect on structural, morphological and optical properties of 2D-MoS2 layers: An experimental and theoretical study." *Optik* 228 (2021): 166166.

[22] Kumari, Sangita, Ajay Chouhan, Om P. Sharma, Sruthi Kuriakose, Sherif Abdulkader Tawfik, Michelle JS Spencer, Sumeet Walia, Hiroyuki Sugimura, and Om P. Khatri. "Structural-defect-mediated grafting of alkylamine on few-layer MoS2 and its potential for enhancement of tribological properties." *ACS applied materials & interfaces* 12, no. 27 (2020): 30720-30730.

[23] Liang, Kangqiang, Shaohua Qu, Yixiao Li, Li-li Tan, and Li Shang. "Surface chemistry regulates the optical properties and cellular interactions of ultrasmall MoS 2 quantum dots for biomedical applications." *Journal of Materials Chemistry B* 9, no. 28 (2021): 5682-5690.

[24] Yang, Fei, Xincheng Cao, Junnan Han, Yue Tao, Zhenguo Zhuo, Le Zhang, Ziyue Zhu, Wenjin Liu, and Yuehua Dai. "First principles study on modulating electronic and optical properties with h-BN intercalation in AlN/MoS2 heterostructure." *Nanotechnology* 33, no. 3 (2021): 035708.

[25] Zhang, Yan-Fang, Jinbo Pan, and Shixuan Du. "Geometric, electronic, and optical properties of MoS2/WSSe van der Waals heterojunctions: a first-principles study." *Nanotechnology* 32, no. 35 (2021): 355705.

[26] Yang, Ke, Tianyu Liu, and Xiao-Dong Zhang. "Bandgap Engineering and Near-Infrared-II Optical Properties of Monolayer MoS2: A First-Principle Study." *Frontiers in Chemistry* 9 (2021): 433.

[27] Xu, Lei, Zhenyun Zhang, Chenchen Wu, Huan Liu, Tao Shen, Yongwan Cao, and Junjie Qi. "In-situ TEM investigation of MoS2 wrinkles and its effects on electrical properties." *Materials Chemistry and Physics* 257 (2021): 123797.

[28] John, Ashby Phillip, Arya Thenapparambil, and Madhu Thalakulam. "Strain-engineering the Schottky barrier and electrical transport on MoS2." *Nanotechnology* 31, no. 27 (2020): 275703.

[29] Chamlagain, Bhim, Udai Bhanu, Shin Mou, and Saiful I. Khondaker. "Tailoring the Potential Landscape and Electrical Properties of 2D MoS2 using Gold Nanostructures of Different Coverage Density." *The Journal of Physical Chemistry C* 124, no. 11 (2020): 6461-6466.

[30] Silver, Eric H. "Monochromatic X-ray systems and methods." U.S. Patent 10,806,946, issued October 20, 2020.

[31] Li, Xiaoshuang, Chengjue Guo, Hongwei Wang, Yeqing Chen, Jiangcong Zhou, Jun Lin, and Qingguang Zeng. "Green emitting Ba1. 5Lu1. 5Al3. 5Si1. 5O12: Ce3+ phosphor with high thermal emission stability for warm WLEDs and FEDs." Ceramics International 46, no. 5 (2020): 5863-5870.

[32] Alharbi, S. R., and A. F. Qasrawi. "Gold and yttertium interfacing effects on the properties of the CdSe/Yb/CdSe nanosandwiched structures." *Current Applied Physics* 18, no. 8 (2018): 946-951.

[33] Gruber, B. "The relationship between reduced cells in a general Bravais lattice." Acta Crystallographica Section A: Crystal Physics, Diffraction, Theoretical and General Crystallography 29, no. 4 (1973): 433-440.

[34] Wada, Masahisa, Takeshi Okano, and Junji Sugiyama. "Allomorphs of native crystalline cellulose I evaluated by two equatorial d-spacings." Journal of Wood Science 47, no. 2 (2001): 124-128.

[35] Gurtin, Morton E., Jorg Weissmüller, and Francis Larche. "A general theory of curved deformable interfaces in solids at equilibrium."hilosophical Magazine A 78, no. 5 (1998): 1093-1109.

[36] Shen, Jiaojiao, Biao Chen, Jie Wan, Jianghua Shen, and Jinshan Li. "Effect of annealing on microstructure and mechanical properties of an Al–Mg-Sc-Zr alloy." Materials Science and Engineering: A 838 (2022): 142821.

[37] Huang, Pinshane Y., Carlos S. Ruiz-Vargas, Arend M. Van Der Zande, William S. Whitney, Mark P. Levendorf, Joshua W. Kevek, Shivank Garg et al. "Grains and grain boundaries in single-layer graphene atomic patchwork quilts." Nature 469, no. 7330 (2011): 389-392.

[38] Godfrey, A., W. Q. Cao, Q. Liu, and N. Hansen. "Stored energy, microstructure, and flow stress of deformed metals." Metallurgical and Materials Transactions A 36 (2005): 2371-2378.

[39] Županović, Paško, Davor Juretić, and Srećko Botrić. "Kirchhoff's loop law and the maximum entropy production principle." Physical Review E 70, no. 5 (2004): 056108.

[40] Labate, G., and L. Matekovits. "Kirchhoff's current law as local cloaking condition: theory and applications." Electronics Letters 52, no. 21 (2016): 1749-1751.

[41] Nasri, S., M. Megdiche, and M. Gargouri. "DC conductivity and study of AC electrical conduction mechanisms by non-overlapping small polaron tunneling model in LiFeP2O7 ceramic." *Ceramics International* 42, no. 1 (2016): 943-951.

[42] Khusayfan, Najla M., A. F. Qasrawi, and Hazem K. Khanfar. "Design and electrical performance of CdS/Sb2Te3 tunneling heterojunction devices." *Materials Research Express* 5, no. 2 (2018): 026303.

[43] Rhoderick, E. H. "Solid-State and Electron Devices." IEE Proc. I 129 (1982): 1-14.

[44] Sze, S. M., and Kwok K. Ng. "Physics of Semiconductor Devices. Hoboken, New Jersey: John Wiley & Sons." Inc.–2007 (2006).

[45] Pearson, G. L., and Walter H. Brattain. "History of semiconductor research." Proceedings of the IRE 43, no. 12 (1955): 1794-1806.

[46] Ziqan, Abdelhalim M., A. F. Qasrawi, Abdulftah H. Mohammad, and N. M. Gasanly. "Thermally assisted variable range hopping in Tl4S3Se crystal." *Bulletin of Materials Science* 38, no. 3 (2015): 593-598.

[47] Qasrawi, A. F. "Effects of photoexcitation on the current transport mechanism in amorphous indium selenide thin films." *Philosophical Magazine* 90, no. 22 (2010): 3027-3035.

[48] Lopez Maldonado, K. L., P. De La Presa, M. A. De La Rubia, P. Crespo, J. De Frutos, A. Hernando, J. A. Matutes Aquino, and J. T. Elizalde Galindo. "Effects of grain boundary width and crystallite size on conductivity and magnetic properties of magnetite nanoparticles." *Journal of nanoparticle research* 16, no. 7 (2014): 1-12.

[49] Bai, Xian-Ming, Yongfeng Zhang, and Michael R. Tonks. "Testing thermal gradient driving force for grain boundary migration using molecular dynamics simulations." *Acta Materialia* 85 (2015): 95-106.

[50] Qasrawi, A. F. "Performance of the Yb/n-CdSe/C tunneling barriers." *Journal of Nanoelectronics and Optoelectronics* 13, no. 10 (2018): 1493-1498.

[51] Chakrabarty, Narayan. "Arsenic toxicity." *Prevention and treatment* 1 (2015): 1-14.

[52] Gutman, V., and K. H. Jack. "The crystal structures of molybdenum trifluoride, MoF3, and tantalum trifluoride, TaF3." *Acta Crystallographica* 4, no. 3 (1951): 244-246.

[53] Whittaker, E. J. W., and R. Muntus. "Ionic radii for use in geochemistry." *Geochimica et Cosmochimica Acta* 34, no. 9 (1970): 945-956.

[54] Okada, K., I. Kimura, and K. Machida. "High rate capability by sulfur-doping into LiFePO 4 matrix." *RSC advances* 8, no. 11 (2018): 5848-5853.

[55] Kawazoe, H., H. Yanagita, Y. Watanabe, and M. Yamane. "Imperfections in amorphous chalcogenides. I. Electrically neutral defects in liquid sulfur and arsenic sulfides." Physical review B 38, no. 8 (1988): 5661.

[56] Tanaka, Keiji. "Photoexpansion in As 2 S 3 glass." Physical Review B 57, no. 9 (1998): 5163.

[57] Tsai, Yi-Chou, Hong-Zhang Chen, Chie-Chieh Chang, Jen-Shiang K. Yu, Gene-Hsiang Lee, Yu Wang, and Ting-Shen Kuo. "Journey from Mo− Mo quadruple bonds to quintuple bonds." Journal of the American Chemical Society 131, no. 35 (2009): 12534-12535.

[58] Harris, Hugh H., Graham N. George, and K. V. Rajagopalan. "High-resolution EXAFS of the active site of human sulfite oxidase: Comparison with density functional theory and X-ray crystallographic results." Inorganic chemistry 45, no. 2 (2006): 493-495.

[59] Steudel, Ralf. "Properties of sulfur-sulfur bonds." Angewandte Chemie International Edition in English 14, no. 10 (1975): 655-664.

[60] Amer, Sultan, Gary Kramer, and Anthony Poë. "Thermal homolytic fission of the Mo-Mo bond in (h5-C5H5) 2Mo2 (CO) 6." Journal of Organometallic Chemistry 209, no. 2 (1981): C28-C30.

[61] Lee, Youngbin, Jinhwan Lee, Hunyoung Bark, Il-Kwon Oh, Gyeong Hee Ryu, Zonghoon Lee, Hyungjun Kim, Jeong Ho Cho, Jong-Hyun Ahn, and Changgu Lee. "Synthesis of wafer-scale uniform molybdenum disulfide films with control over the layer number using a gas phase sulfur precursor." Nanoscale 6, no. 5 (2014): 2821-2826.

[62] Steudel, Ralf. "Properties of sulfur-sulfur bonds." Angewandte Chemie International Edition in English 14, no. 10 (1975): 655-664.

[63] Tverjanovich, A., K. Rodionov, and E. Bychkov. "Raman spectroscopy of glasses in the As–Te system." Journal of Solid State Chemistry 190 (2012): 271-276.

[64] Ashraf, Shakeel, Viviane Forsberg, Claes G. Mattsson, and Göran Thungström. "Thermoelectric properties of n-type molybdenum disulfide (MoS2) thin film by using a simple measurement method." *Materials* 12, no. 21 (2019): 3521.

[65] Tiong, Kwong-Kau, P. C. Liao, C. H. Ho, and Y. S. Huang. "Growth and characterization of rhenium-doped MoS2 single crystals." *Journal of crystal growth* 205, no. 4 (1999): 543-547.

[66] Baran, Özlem. "Adhesion and fatigue resistance of Ta-doped MoS2 composite coatings deposited with pulsed-DC magnetron sputtering." *Journal of adhesion science and Technology* 31, no. 11 (2017): 1181-1195.

[67] Li, Jinfeng, Phi HQ Pham, Weiwei Zhou, Ted D. Pham, and Peter J. Burke. "Carbon-nanotube–electrolyte interface: quantum and electric double layer capacitance." *ACS nano* 12, no. 10 (2018): 9763-9774.

[68] Chen, Changyao, Damián H. Zanette, David A. Czaplewski, Steven Shaw, and Daniel López. "Direct observation of coherent energy transfer in nonlinear micromechanical oscillators." *Nature communications* 8, no. 1 (2017): 1-7.

[69] Pan, Janet L., J. E. McManis, L. Grober, and J. M. Woodall. "Gallium-arsenide deep-level tunnel diode with record negative conductance and record peak current density." *Solid-State Electronics* 48, no. 10-11 (2004): 2067-2070.

[70] Qasrawi, Atef, and Maram Taleb. "Enhancement of electrical performance of ZnSe thin films via Au nanosandwiching." (2020) , 38(1), 174-180.

[71] Kendig, M., F. Mansfeld, and S. Tsai. "Determination of the long term corrosion behavior of coated steel with AC impedance measurements." *Corrosion Science* 23, no. 4 (1983): 317-329.

الملخص

في هذه الرسالة ، تم تطعيم مساحيق كبريتيد الموليبدينوم بالزرنيخ بواسطة تقنية تفاعل الحالة الصلبة. تمت دراسة المساحيق المطعمة بواسطه حيود الأشعة السينية والمسح المجهري الإلكتروني والتحليل الطيفي للأشعة السينية المشتتة للطاقة والتحليل الطيفي للمقاومة وتقنيات خصائص الجهد والتيار. تمت عمليه التطعيم وفقًا للصيغة التجريبية $MoAs_xS_2$. يتنوع محتوى (x) من الزرنيخ في العينات في حدود 0.00-0.80. تم بعد ذلك تلبيد العينات المخدرة عند 200 درجة مئوية لمدة 20 ساعة في الهواء. ويلاحظ أنه كلما زاد محتوى الزرنيخ في العينات ، كانت أحجام البلورات أصغر ، وكلما زاد الإجهاد الميكروي ، زادت كثافة الخلل وزادت نسب أخطاء التراص. ولوحظ ان تلبيد العينات عند 200 درجة مئوية لم يغير اتجاه اختلاف المعلمات الهيكلية. بالإضافة إلى ذلك ، لوحظ أن الزيادة في محتوى As في مساحيق MoS_2 تؤدي إلى زيادة المسام. بدأ تراكم الحبوب في الظهور على سطح العينات حيث تجاوز x=0.40. من ناحية أخرى ، أظهر القياس الكهربائي أن المقاومة الكهربائية تزداد مع زيادة المحتوى في العينات. أظهرت قياسات المقاومة الكهربائية المعتمدة على درجة الحرارة أن طاقة التنشيط لحاملات الشحنات الحرة في المناطق التي يسود فيها الانبعاث الحراري تزداد. في المناطق التي يهيمن فيها القفز على نطاقات متغيرة على درجة اضطراب الحالة الإلكترونية وزادت مسافة التنقل المتغيرة في حين انخفضت كثافة الحالات الموضعية بالقرب من مستويات فيرمي مع زيادة محتوى الزرنيخ. علاوة على ذلك ، أظهرت دراسات التحليل الطيفي للمقاومة أن عينات MoS_2 المطعمة وغير المطعمة يمكن أن تظهر تأثير التوصيل السلبي. تأثير التوصيل السلبي مفيد لتصنيع أجهزة الميكروويف المستخدمة في تكنولوجيا الاتصالات.